Investigation of airfoil leading edge separation control with nanosecond plasma actuator

J. G. Zheng,[1,*] Y. D. Cui,[1] Z. J. Zhao,[1] J. Li,[1] and B. C. Khoo[1,2,†]
[1]*Temasek Laboratories, National University of Singapore, Singapore 117411*
[2]*Department of Mechanical Engineering, National University of Singapore, Singapore 119260*
(Received 28 June 2016; published 22 November 2016)

A combined numerical and experimental investigation of airfoil leading edge flow separation control with a nanosecond dielectric barrier discharge (DBD) plasma actuator is presented. Our study concentrates on describing dynamics of detailed flow actuation process and elucidating the nanosecond DBD actuation mechanism. A loose coupling methodology is employed to perform simulation, which consists of a self-similar plasma model for the description of pulsed discharge and two-dimensional Reynolds averaged Navier-Stokes (RANS) equations for the calculation of external airflow. A series of simulations of poststall flows around a NACA0015 airfoil is conducted with a Reynolds number range covering both low and high Re at $\mathrm{Re} = (0.05, 0.15, 1.2) \times 10^6$. Meanwhile, wind-tunnel experiment is performed for two low Re flows to measure aerodynamic force on airfoil model and transient flow field with time-resolved particle image velocimetry (PIV). The PIV measurement provides possibly the clearest view of flow reattachment process under the actuation of a nanosecond plasma actuator ever observed in experiments, which is highly comparable to that predicted by simulation. It is found from the detailed simulation that the discharge-induced residual heat rather than shock wave plays a dominant role in flow control. For any leading edge separations, the preliminary flow reattachment is realized by residual heat-induced spanwise vortices. After that, the nanosecond actuator functions by continuing exciting flow instability at poststall attack angles or acting as an active trip near stall angle. As a result, the controlled flow is characterized by a train of repetitive, downstream moving vortices over suction surface or an attached turbulent boundary layer, which depends on both angle of attack and Reynolds number. The advection of residual temperature with external flow offers a nanosecond plasma actuator a lot of flexibility to extend its influence region. Animations are provided for baseline flow and that subjected to plasma control at two typical Reynolds numbers.

DOI: 10.1103/PhysRevFluids.1.073501

I. INTRODUCTION

Using various control means to suppress partially or massively separated flow over a large aspect ratio wing and extend a usable range of angle of attack (AoA) is of great importance in both science and engineering. Among these control methods, the dielectric barrier discharge (DBD) plasma actuator as sketched in Fig. 1(a) has been established as an effective actuation technique for many aerodynamic bodies. A specific DBD actuator usually consists of two electrodes mounted on opposite sides of a dielectric layer. When an alternating current (AC) waveform is supplied, air over the buried electrode is weakly ionized. The collision between neutral air particles and charged species induces a near surface jet, from which the control authority of an AC plasma actuator stems. However, the low jet velocity, which is typically a few meters per second [1], may limit the actuator's application in high-speed flow regime.

*tslzhen@nus.edu.sg
†Corresponding author: mpekbc@nus.edu.sg

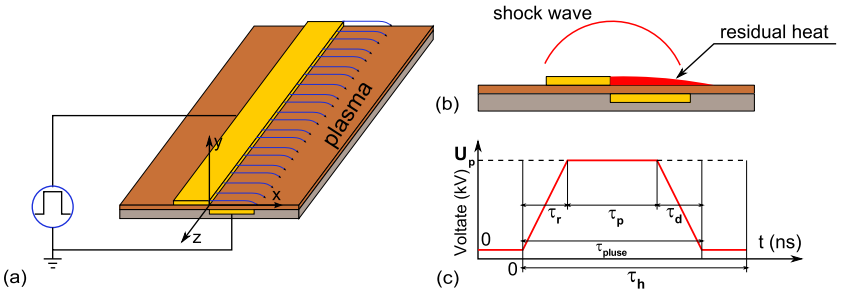

FIG. 1. Schematics of a nanosecond (ns) dielectric barrier discharge (DBD) actuator (a), its side view (b), and high voltage pulse (c).

Recently, as an alternative to AC plasma actuation, a nanosecond (ns) DBD actuator has attracted increasing attention due to its great potential to control flow around aerodynamic bodies at high cruise speed. The two devices have almost the same configuration except that the nanosecond one is driven by repetitive high-voltage pulses with typical rise and decay time of several to tens of nanoseconds, as sketched in Fig. 1(c), which leads to fundamentally different working principles between them. As pulse duration is very short, part of electrical energy associated with each pulse discharge is converted into gas heating within the discharge region in a short time period of less than 1 μs [2,3]. This fast heating results in appreciable temperature and pressure increase in near-surface gas, which in turn causes the generation of a microshock wave; see Fig. 1(b). Compared with AC discharge, nanosecond DBD induces much smaller flow velocity in neutral gas and actually functions via a Joule heating effect and the resulting shock wave as well as residual temperature in the discharge volume; refer to Fig. 1(b).

Several characterization studies have been conducted to gain a basic understanding of nanosecond DBD actuator. For example, the work by Takashima *et al.* [4] is focused on the visualization of a discharge-induced shock wave using a Schlieren imaging system as well as of plasma evolution. Benard *et al.* [5] examined the optical and electrical characteristics of plasma sheet in quiescent air. Effect of a pulse polarity on discharge is studied in Ref. [6]. In these works, more attention is paid to the electrical characteristics of discharge. On the other hand, dynamics of a shock wave produced by discharge is systematically investigated by the authors [3,7]. It is found that disturbance introduced by shock propagation through air is extremely localized in space as well as highly transient in time. Meanwhile, experiment in Ref. [8] suggests that residual heat due to multiple pulse discharges at high frequency can trigger laminar-to-turbulent transition in a flat plate boundary layer.

The nanosecond DBD has demonstrated its control authority in a wide range of flows, from subsonic flow control with free shear layer [9–15] to supersonic drag reduction [16]. For conciseness, the following review of previous works is concentrated on those most pertinent to flow separation control over airfoil such as that sketched in Fig. 2 (with actuator arrangement shown in Fig. 3). In Ref. [2] this device was first reported to be able to efficiently control airfoil leading edge separation, lift, and drag coefficient for a NACA0015 profile with Mach number between 0.05 and 0.85. Later, the efficacy of a nanosecond actuator for suppressing separated flow around an energy efficient transport (EET) airfoil has been illustrated with Reynolds number (Re) up to 1×10^6 (62 m/s) [10]. The potential of this device was further demonstrated over an 8-inch chord NACA0015 airfoil with Mach and Reynolds numbers being as high as 0.26 (93 m/s) and 1.15×10^6, respectively [9]. The work in Ref. [11] is focused on the evaluation of influence of pulse voltage amplitude and repetitive frequency on control performance for a GÖ 387 airfoil flow. A comparison between AC and nanosecond actuation for prevention of leading edge stall on an EET airfoil was conducted in Ref. [14].

There is little doubt that the above experiments and those not referenced here have shed some light on the phenomenological behaviors of nanosecond discharge in different flow control cases.

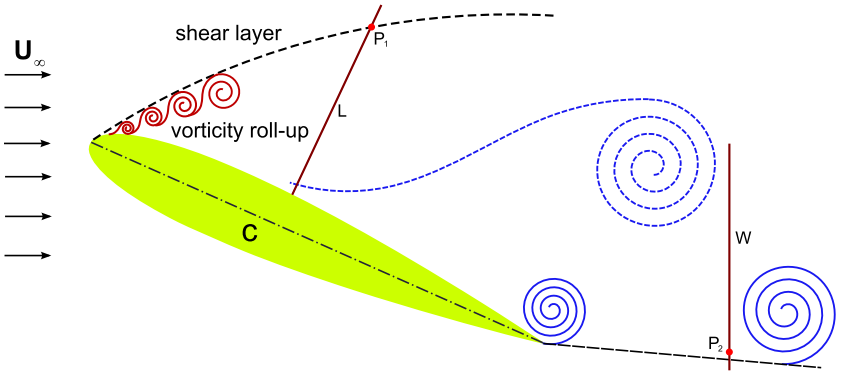

FIG. 2. Schematic illustration of vortex structure behind a NACA0015 airfoil at high angle of attack (AoA). Some small roll-up vortices are present near shear layer for low Reynolds number flow. Lines L, W are two monitoring lines in shear layer and wake, respectively. Characteristic locations P_1 and P_2 correspond to the maximum root mean square (rms) y velocity along lines L and W, respectively.

However, given the complexity of flow in a poststall regime and nature of the experiment, transient flow field and some quantities of interest cannot be measured directly, either due to their intrinsic nature or due to limitations of experimental instrument, and therefore a detailed actuation process has not been displayed clearly in any study. We thus believe that clarification of the following problems through numerical simulation and well-designed experiment will constitute a basis for a thorough understanding of the nanosecond plasma control mechanism: (i) The evolution of flow field under plasma control, especially the topological change of flow structures such as separated shear layer, has not been captured. (ii) A detailed description of the process whereby thermal energy deposition interplays with external flow needs to be provided to reveal which feature (i.e., shock or residual heat or both in combination) dominates nanosecond DBD control authority.

Given this background, the present study attempts to investigate dynamics of flow control process over a NACA0015 airfoil by both numerical and experimental means. The simulation and experiment complement each other, and information missing from experiment will be provided by calculation to build up a more complete picture of discharge-flow interaction.

Up to now, most of available experimental studies in this field are devoted to the examination of aerodynamic characteristics of various wing sections with and without nanosecond plasma control.

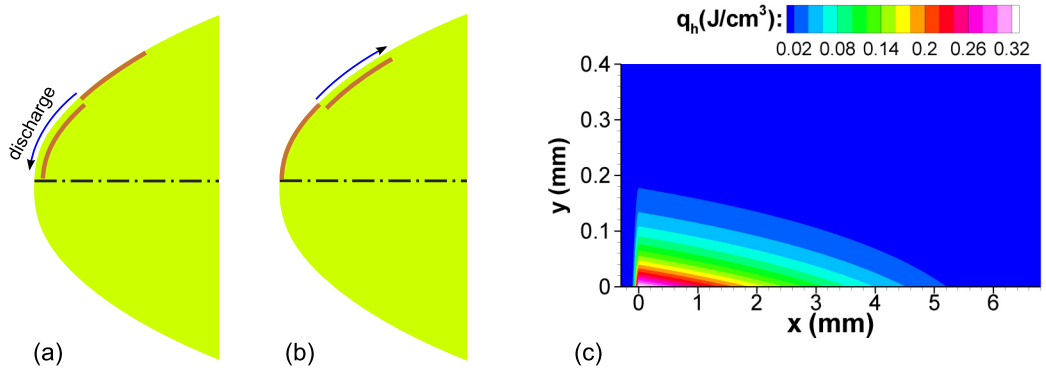

FIG. 3. Plots (a) and (b) illustrate two arrangements of plasma actuator on the leading edge of NACA0015 airfoil shown in Fig. 2. In plot (c), the predicted heating energy density, $q_h(x,y) = \eta \cdot q_{\text{couple}}(x,y)$, for voltage pulse with $U_p = 20$ kV is depicted.

Although airfoil performance improvement by plasma actuation is highlighted in these works, dynamic particle image velocimetry (PIV) images for flow control have not been acquired. This motivated us to conduct wind-tunnel experiment for low Reynolds number flow around a NACA0015 airfoil. In addition to measuring aerodynamic load (lift and drag) on an airfoil model, the transient velocity fields of baseline flow and that subjected to control are acquired using a dynamic PIV system. The PIV flow visualization provides a clear view of separated flow and its evolution under plasma control. However, PIV measurement is not adequate to capture fine flow structures near the airfoil surface, for which we resort to numerical simulation.

Nevertheless, numerical simulation of deep stall flow is challenging. So far, only two classes of methods are developed for simulation of nanosecond DBD-based flow control. The first category of methods is based on close coupling between two-dimensional (2D) plasma kinetic model and equations governing external airflow [17–19], where interaction between plasma discharge and external flow is taken into account. However, computation with this type of method is extremely computationally expensive due to the disparate temporal and spatial scales of airflow and plasma. On the other hand, some semiempirical models have been proposed to overcome the above-mentioned shortcomings [2,20–22]. These models have to be tuned against experimental data and are obviously less accurate than 2D kinetic formulation.

Here a compromise is reached by employing the simplified self-similar plasma model [3,23], which is loosely coupled with 2D Reynolds averaged Navier-Stokes (RANS) equations. As resolution of plasma kinetics is not required, computational cost can be reduced significantly, while the key effect of discharge on flow can be modeled properly. For the external flow, large eddy simulation (LES) and RANS calculation are two possible choices. Given the huge computational cost of LES at high Re [24], a 2D RANS model is used here. As will be seen later, our 2D RANS simulation with Reynolds stress turbulence model (RSM) can provide a satisfactory prediction of flow separation and its control for comparison with available experimental data, not only in qualitative flow structure but also in quantitative statistics of time-dependent flow variables. We thus believe that our results can at least provide a qualitative understanding of physics of nanosecond plasma actuation, which is also the purpose of this paper.

The paper is organized as follows. In Sec. II, plasma and flow models for simulation are presented. In Sec. III we describe experimental setup for low Re flow. The results and discussion are provided in Sec. IV. Comparison of our numerical results and experimental measurement is presented in Sec. IV B, whereas numerical results for high Re flow are presented in Sec. IV C. The conclusion is given in Sec. V.

II. MODELING AND NUMERICS

A. Self-similar plasma model

As mentioned earlier, because of the wide disparity in characteristic time and space scales between plasma discharge and external flow, a large computational resource is required to fully model the discharge and its interaction with flow. For this reason, in the current study, a lower-order, self-similar model of surface discharge is employed and loosely coupled with a compressible Navier-Stokes equation solver. As the discharge occurs on a nanosecond time scale during which the external flow essentially has no response, the resolution of plasma kinetics is not required. This approximation leads to a significant reduction of computational cost. In this subsection, this method will be briefly described, and more details on its verification and validation can be found in Refs. [3,23].

1. Plasma model

The quasi-one-dimensional, self-similar model of surface nanosecond plasma discharge, which is sketched in Fig. 4(a), is derived based on drift-diffusion equations with some insignificant physical mechanisms on a nanosecond time scale neglected [23]. The resulting model consists of equations describing parallel and perpendicular components of a near wall electric field, E_x and E_y, electron

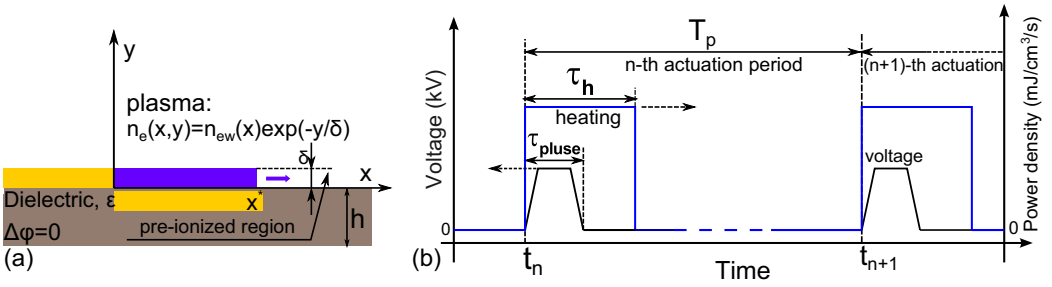

FIG. 4. Plot (a) shows the schematic of a nanosecond pulse DBD. In plot (b), time variation of pulse voltage (left y axis) and associated power density (right y axis) in an actuation period are sketched. The pulse duration τ_{pulse} and heating time τ_h in plot (b) are greatly magnified for clarity.

and ion densities, n_{ew} and n_{iw}, and plasma layer thickness parameter, $\lambda = 1/\delta$, such that $n_e(x,y) = n_{ew}(x)\exp(-\lambda y) = n_{ew}(x)\exp(-y/\delta)$:

$$
\begin{aligned}
&\frac{dE_x}{d\xi} = -\frac{3}{2}\frac{E_x^2}{\varphi} - \frac{e}{\varepsilon_0}(n_i - n_e), \quad \frac{dE_y}{dy} = \frac{3}{2}\frac{E_x^2}{\varphi},\\
&\frac{dE_y}{d\xi} = \frac{dE_x}{dy} = \frac{\varepsilon}{h}E_x - \frac{en_e\mu_e E_y}{\varepsilon_0 V},\\
&\frac{dn_e}{d\xi} = \frac{\nu n_e + \mu_e n_e (dE_x/d\xi) + 3\mu_e n_e\left(E_x^2/\varphi\right)/2 - \mu_e\lambda n_e E_y}{V - \mu_e E_x},\\
&\frac{dn_i}{d\xi} = \frac{\nu n_e}{V},\\
&\frac{d\lambda}{d\xi} = \frac{a}{V}\frac{d\nu}{dy}\frac{d(\ln\nu)}{d(\ln E)}.
\end{aligned}
\tag{1}
$$

In system (1), V is the ionization wave speed and $\xi = x + Vt$ is the introduced self-similar variable; φ denotes the electric potential at the wall such that $E_x = -d\varphi/d\xi$; h and ε are the dielectric thickness and dielectric constant, respectively; $\mu_e = 300 \times [760/P(\text{Torr})]\,\text{cm}^2\text{s}^{-1}$ denotes the electron mobility, $\nu = \alpha\mu_e E$ is the ionization frequency with α being the ionization coefficient, and n_{e0} and $n_{e\infty}$ are the initial and asymptotic electron densities behind the wave, respectively. The value of parameter a is determined from current continuity relation across the ionization wave front, $\int_{|\rho|>0} j_{yw}\,d\xi + \int_0^\infty j_x\,dy|_{\rho=0} = 0$, where the first integral that represents transverse current at the surface is evaluated over the space charge region with $|\rho| > 0$, while the second integral that denotes axial current is evaluated at the boundary of the space charge region with $|\rho| \to 0$. The ionization coefficient α is obtained by fitting an experimental Townsend ionization coefficient in nitrogen and is assumed to be a function of the local reduced electric field value, E/p [23]:

$$
\left(\frac{\alpha}{p}\right)_{N_2} = \begin{cases} \frac{900}{E/p}\exp\left(-\frac{315}{E/p}\right)\text{cm}^{-1}, & E/p < 100\,\text{V cm}^{-1}\,\text{Torr}^{-1} \\ 12\exp\left(-\frac{342}{E/p}\right)\text{cm}^{-1}, & 100 < E/p < 800\,\text{V cm}^{-1}\,\text{Torr}^{-1}. \end{cases}
\tag{2}
$$

Note that the ionization coefficient of air is close to that of nitrogen. For nanosecond plasma discharge in air, Eq. (2) can be replaced with an approximate ionization coefficient expression.

As shown in Fig. 4(a), the derivation of system (1) is based on the assumption that the space charge ahead of ionization wave is present, which creates the electric field and is approximated as a thin charged layer of thickness h with dielectric constant ε over the buried electrode. The initial electric field and potential in the weakly preionized air far ahead of the ionization wave front are

given as

$$
\begin{aligned}
&E_y(\xi) = E_y^*\left(\frac{h}{\xi^* - \xi}\right)^2, \quad E_x(\xi) = E_y^*\frac{2}{\varepsilon}\left(\frac{h}{\xi^* - \xi}\right)^3,\\
&\frac{dE_y}{d\xi} = \frac{dE_x}{dy} = \frac{\varepsilon}{h}E_x, \quad \frac{dE_x}{d\xi} = -\frac{dE_y}{dy} = -\frac{3}{2}\frac{E_x^2}{\varphi},\\
&\varphi(\xi) = -E_y^*\left(\frac{h}{\xi^* - \xi}\right)^2\frac{h}{\varepsilon}, \quad n_e(\xi) = n_i(\xi) = n_0.
\end{aligned}
\tag{3}
$$

where E_y^* is the peak transverse electric field at $\xi = \xi^*$.

From the given peak pulse voltage U_p and rise time τ_r as sketched in Fig. 1(c), which are strongly load-dependent in experiment and satisfy the relation $dU/dt \approx E_{x\infty}V$ with $E_{x\infty}$ being the asymptotic quasisteady-state value of the axial electric field after the wave, electric field components, E_x and E_y, electron density n_e, plasma layer thickness δ, and ionization wave propagation distance L can be predicted by numerically solving system (1). Finally, the rate of total coupled energy per unit actuator length in the spanwise direction, i.e., the z direction as shown in Fig. 1(a), can be obtained and is given by

$$
\frac{dQ_{\text{couple}}(\xi)}{d\xi} = \frac{dQ_{\text{forward}}(\xi)}{d\xi} + \frac{dQ_{\text{store}}(\xi)}{d\xi},
\tag{4}
$$

where

$$
\frac{dQ_{\text{forward}}(\xi)}{d\xi} = \int_0^{\xi}\frac{d\xi'}{V}\int_0^{\infty}\vec{j}\cdot\vec{E}\,dy, \quad \frac{dQ_{\text{store}}(\xi)}{d\xi} = \frac{\sigma^2(\xi)h}{2\varepsilon\varepsilon_0}
\tag{5}
$$

with $\sigma(\xi)$ being the charge density on dielectric surface and $\vec{j}\cdot\vec{E}$ being the power coupled per unit volume.

The total coupled energy in the whole discharge including the forward and reverse breakdown waves, $\widehat{\mathbf{Q}}_{\text{couple}}$, is obtained by integrating $dQ_{\text{couple}}(\xi)/d\xi$ in Eq. (4) over space and time. It is the sum of energy coupled to the plasma in the forward breakdown phase of the discharge during which voltage is rising, $\widehat{\mathbf{Q}}_{\text{forward}}$, and energy stored by charging the dielectric surface in this phase, $\widehat{\mathbf{Q}}_{\text{store}}$, i.e., $\widehat{\mathbf{Q}}_{\text{couple}} = \widehat{\mathbf{Q}}_{\text{forward}} + \widehat{\mathbf{Q}}_{\text{store}}$.

Consider the computation of $\widehat{\mathbf{Q}}_{\text{forward}}$. We first need to evaluate the integral on the right-hand side (RHS) of the first subequation in Eq. (5). The integration is performed by assuming that we are "fixed" at a certain axial station x; refer to Fig. 4(a). In the notations of this equation, ξ is 0 when the ionization front just arrives at this station. As the ionization front passes this location, ξ is increasing with time as Vt. Therefore, $d\xi'$ is simply $V\,dt$. Thus, the outer integral is over time at a fixed station x. The inner integral of $\vec{j}\cdot\vec{E}$ over y gives the time-dependent power over a certain vertical cross section of the ionization wave, in W/cm^2 (per unit width in x direction). Note that the 2D geometry used in the present work assumes that plasma properties in the z direction (perpendicular to the page) are uniform. This time-dependent power needs to be integrated over time to calculate energy coupled at the fixed station x due to the wave passage, which is what the outer integral does. The outer integration is from the moment the ionization front arrives at x to the moment the voltage on upper electrode stops increasing and the wave stops propagating. As a result, $dQ_{\text{forward}}(\xi)/d\xi$ in Eq. (5) simply becomes $dQ_{\text{forward}}(x)/dx$, which is the x-dependent energy coupled at location x in the time interval between the moment the ionization front arrives there and the moment the wave stops. Denote $dQ_{\text{forward}}(x)/dx$ by $P_{\text{forward}}(x)$. To calculate energy coupled over the length of the entire wave, we integrate $dQ_{\text{forward}}(x)/dx$ one more time over x, giving $\widehat{\mathbf{Q}}_{\text{forward}}$ in mJ/cm:

$$
\int_0^L \frac{dQ_{\text{forward}}(x)}{dx}\,dx = \int_0^L P_{\text{forward}}(x)\,dx = \widehat{\mathbf{Q}}_{\text{forward}}.
\tag{6}
$$

Now look at $\widehat{\mathbf{Q}}_{\text{store}}$. By assuming that the charge stored on the dielectric surface during the forward breakdown phase of the discharge is removed from the surface during the reverse breakdown phase, we simply get $\widehat{\mathbf{Q}}_{\text{reverse}} = \widehat{\mathbf{Q}}_{\text{store}} = \widehat{\mathbf{Q}}_{\text{forward}}$.

Therefore, the total energy coupled over the entire region swept by the ionization wave in the whole discharge is given by

$$\widehat{\mathbf{Q}}_{\text{couple}} = \widehat{\mathbf{Q}}_{\text{forward}} + \widehat{\mathbf{Q}}_{\text{store}} = 2\widehat{\mathbf{Q}}_{\text{forward}}. \tag{7}$$

As plasma is assumed to be uniform in the z direction (perpendicular to the page), $\widehat{\mathbf{Q}}_{\text{couple}}$ denotes the coupled energy per unit actuator length in the spanwise direction.

Obviously, $\widehat{\mathbf{Q}}_{\text{couple}}$ is obtained by integrating both spatial and temporal information. However, a reverse procedure is performed here to get the semiempirical, spatial-temporal distribution of coupled energy and finally the power density. When a physically reasonable power density is added to the energy equation for external flow as source term accounting for gas heating, a shock wave, whose structure is comparable to the experimentally observed shock geometry, will be generated. This is the reason why we redistribute the predicted total coupled energy $\widehat{\mathbf{Q}}_{\text{couple}}$ and further calculate the power density in a semiempirical manner stated below. To get the desired power density, a semiempirical approach is first used to redistribute the predicted total coupled energy $\widehat{\mathbf{Q}}_{\text{couple}}$ in the discharge region as sketched in Fig. 1(b) to obtain the spatial distribution of coupled energy, $q_{\text{couple}}(x,y)$. Then $q_{\text{couple}}(x,y)$ is multiplied by thermalization factor η and divided by a characteristic time τ_h, giving the power density $\chi(x,y,t)$ for gas heating, i.e., the spatial-temporal distribution of thermalized energy.

The coupled energy density $q_{\text{couple}}(x,y)$ has to be determined first. Look at Eq. (5) and return to our earlier discussion on the coupled energy at location x, $P_{\text{forward}}(x)$. The axial (x) dependence of $P_{\text{forward}}(x)$ is quadratic, because of approximately linear rise of $\vec{j}\cdot\vec{E}$ with distance behind the ionization front. Keeping this in mind and adding assumed dependence on the vertical coordinate y, we can establish a semiempirical expression for the coupled energy density,

$$q_{\text{couple}}(x,y) = f(\widehat{\mathbf{Q}}_{\text{couple}}, x/L)\exp(-y/\delta), \tag{8}$$

where $f(\widehat{\mathbf{Q}}_{\text{couple}}, x/L)$ is a quadratic function of x/L. The integral of $q_{\text{couple}}(x,y)$ over the discharge region in the x-y plane recovers the total coupled energy,

$$\iint_{\Omega} q_{\text{couple}}(x,y)\,dx\,dy = \widehat{\mathbf{Q}}_{\text{couple}}, \tag{9}$$

where Ω denotes the discharge region. Experimental data indicates that about 35% of the coupled electrical energy is converted into fast gas heating [23]. Multiplying $q_{\text{couple}}(x,y)$ by thermalization factor $\eta = 0.35$ gives the net gas heating energy density,

$$q_h(x,y) = \eta \cdot q_{\text{couple}}(x,y). \tag{10}$$

Such a thermalized energy density map for $U_p = 20$ kV is illustrated in Fig. 3(c).

The predicted shape of shock from a discharge depends on the spatial variation of heating energy density like that depicted in Fig. 3(c). Therefore, the primary purpose of redistributing the total coupled energy $\widehat{\mathbf{Q}}_{\text{couple}}$ (and also the thermalized energy $\widehat{\mathbf{Q}}_h = \eta \cdot \widehat{\mathbf{Q}}_{\text{couple}}$) is to obtain a reasonable distribution of thermalized energy $q_h(x,y)$, which can produce a shock wave whose geometry closely matches that observed in experiment, as shown in Figs. 25(a) and 25(b) where experimental and numerical Schlieren images for the shock wave arising from a single pulse discharge in quiescent air are compared.

2. Coupling with external flow solver

The thermalized energy is assumed to be absorbed by neutral air for heating during a characteristic time τ_h, and therefore power density $\chi(x,y,t)$ needs to be determined. The simplest way to get

$\chi(x,y,t)$ is to divide the heating energy density $q_h(x,y)$ by τ_h. This leads to power density $\chi(x,y,t)$ in mJ/cm^3/s in the nth flow actuation period,

$$\chi(x,y,t) = \begin{cases} q_h(x,y)/\tau_h, & t_n < t \leqslant t_n + \tau_h \\ 0, & t_n + \tau_h < t \leqslant t_n + T_p, \end{cases} \tag{11}$$

where t is the physical time measured from the beginning of the first pulse, while t_n is corresponding to the moment when nth actuation starts with T_p denoting the actuation period and $f = 1/T_p$ being the discharge frequency. Apparently, the integral of power density $\chi(x,y,t)$ over time and then over the discharge volume yields the thermalized energy:

$$\iint_\Omega dx\,dy \int_{t_n}^{t_n+\tau_h} \chi(x,y,t)\,dt = \iint_\Omega q_h(x,y)\,dx\,dy = \widehat{\mathbf{Q}}_h = \eta \cdot \widehat{\mathbf{Q}}_{\text{couple}}. \tag{12}$$

$\chi(x,y,t)$ is then added to energy equation for external flow in system (13) as source term to represent the gas heating effect by the discharge.

As sketched in Fig. 4(b), $\chi(x,y,t)$ is time-dependent at location (x,y). In each flow actuation period, say, nth period between t_n and t_{n+1}, the gas heating occurs only in the short heating time, i.e., $t_n < t \leqslant t_n + \tau_h$. Beyond $t_n + \tau_h$, $\chi(x,y,t)$ is 0. This procedure is repeated in each period.

Note that the heating time τ_h is usually larger than the pulse duration τ_{pulse}, as sketched in Fig. 4(b). This is consistent with experimental observation. Experiments in Refs. [25,27] suggest that the temperature of near surface gas is sill rising after a discharge has finished. In our previous work [3], the value of τ_h is determined to be 350 ns by comparing the predicted and measured instantaneous shock location in a single pulse discharge and used in this study.

In Appendix 1, the self-similar plasma model is validated against experiment by numerically reproducing a single pulse discharge in quiescent air. As shown in Fig. 25, the qualitative shock wave shape predicted by our simulation closely matches its experimental counterpart. This demonstrates that the introduced semiempirical coupled energy distribution function $q_{\text{couple}}(x,y)$ and power density expression $\chi(x,y,t)$ are reasonable.

3. "Slow" heating

One uncertainty in the modeling of nanosecond plasma discharge with system (1) is that a possible additional "slow" heating and temperature rise in plasma is not accounted for. Some recent experiments demonstrate a two-stage energy thermalization mechanism in nanosecond pulse discharge in quiescent air [25–27]. It is shown that the "fast" energy thermalization and temperature rise in plasma, occurring on time scale $\sim$0.1–1 μs and resulting primarily from collisional quenching of excited electronic states of N_2 molecules by O_2, is followed by an additional slow heating procedure occurring on a much longer time scale of $\sim$200 μs, caused by N_2 vibrational relaxation by O atoms in air. The fast heating produces a shock wave and is well modeled by the current self-similar plasma model (1). In contrast, the gradual gas heating in the second stage does not generate a compression wave and this slow energy thermalization is not incorporated into our simulation. Experimental images reveal that the near surface plasma consists of individual filaments in spanwise direction. Compression wavelets, which appear to be generated by these individual surface streamers or discharge filaments, quickly coalesce into a large-scale 2D shock wave at a short distance away from the dielectric surface, in agreement with the Huygens principle. This is the justification for the adopted 2D assumption in the modeling of plasma discharge and associated fast heating in the present work. However, this assumption may not hold for the slow heating as the associated "later" perturbations appear to correlate with the individual filaments and to be localized and random, exhibiting 3D characteristics. The possible influence of the slow heating on flow control will be discussed in Sec. IV B 2. As will be seen later, the slow energy thermalization is thought to be of secondary importance for the poststall flow separation control and therefore can be neglected in this study. Unless otherwise stated, the slow heating is ignored in this paper.

B. Computational modeling of airflow

1. Reynolds-averaged Navier-Stokes equations

Neutral airflow is assumed to be turbulent and modeled by compressible two-dimensional Favre and Reynolds-averaged Navier-Stokes equations,

$$\begin{aligned}
&\frac{\partial \rho}{\partial t}+\frac{\partial}{\partial x_i}(\rho v_i)=0,\\
&\frac{\partial}{\partial t}(\rho v_i)+\frac{\partial}{\partial x_j}(\rho v_j v_i)=-\frac{\partial p}{\partial x_i}+\frac{\partial}{\partial x_j}(\tau_{ij}-\rho\overline{v_i'' v_j''}),\\
&\frac{\partial}{\partial t}(\rho E)+\frac{\partial}{\partial x_j}(\rho v_j H)=\frac{\partial}{\partial x_j}\left(\kappa\frac{\partial T}{\partial x_j}-\rho\overline{v_j'' h''}+\overline{\tau_{ij} v_i''}-\frac{1}{2}\rho\overline{v_j'' v_k'' v_k''}\right)\\
&\qquad\qquad+\frac{\partial}{\partial x_j}[v_i(\tau_{ij}-\rho\overline{v_i'' v_j''})]+\chi(x,y,t). \qquad (13)
\end{aligned}$$

In the above equations, ρ, p, T, v_i, and τ_{ij} are the Favre- or Reynolds-averaged density, pressure, temperature, velocity component in x_i coordinate and stress tensor, respectively. The quantities with superscript $''$ represent turbulent fluctuations and $-$ denotes averaging. The Favre-averaged total energy E and enthalpy H are given by $E=e+v_i v_i/2+k$ and $H=e+p/\rho+v_i v_i/2+k$, respectively, with the turbulent kinetic energy, k, defined as $k=\overline{v_k'' v_k''}/2$. Air is assumed to behave like a calorically perfect gas, for which the ideal gas equation of state takes the form $p=\rho RT$ where R denotes the specific gas constant and takes a value of 287.

The system of partial differential equations (13) results from the application of Favre and Reynolds averaging to flow variables in the instantaneous compressible Navier-Stokes equations and is referred to as unsteady Reynolds-averaged Navier-Stokes (RANS) equations for simplicity. It should be noted that system (13) together with an ideal gas equation of state is an open set of partial differential equations which contains a few unknown correlation terms. Obtaining the closed form of the equation system depends on adoption of proper turbulence model, which will be discussed in the next subsection.

2. Choice of turbulence model

Actually, closure of the RANS equations system (13) reduces to modeling of Reynolds stress $\tau_{ij}^R=-\rho\overline{v_i'' v_j''}$ as additional unknown parts introduced in Eq. (13) can be neglected or modeled [24].

There are two major ways to approximate the Reynolds stress tensor. The most popular and easiest approach is based on eddy viscosity or the Boussinesq hypothesis. The resulting RANS model expressed in terms of averaged flow variables takes exactly the same form as the instantaneous Navier-Stokes equations except that total dynamic viscosity coefficient μ and thermal conductivity coefficient κ are defined as the sum of a laminar and a turbulent component, respectively. Among various Boussinesq hypothesi- based models, three approaches, i.e., Spalart-Allmaras (SA), $k-\varepsilon$ and $k-\omega$ shear stress transport (SST) models, are widely used.

By contrast, in second-order closures, Reynolds stress is computed directly by solving transport equations for each term in the Reynolds stress tensor. A representative example is Reynolds stress model (RSM) where an additional equation for dissipation rate along with those for stresses has to be solved. As isotropic eddy-viscosity hypothesis is abandoned and the influence of geometric and flow features on turbulence is taken into account, RSM has greater potential to produce a more accurate predication for complex flows. However, this does not mean that the Reynolds stress model is superior to the simpler ones in the calculation of all classes of flows.

In the Reynolds-averaged computation of massively separated flow around an airfoil, especially poststall flow, choosing a proper turbulence model is an extremely delicate issue. The flow pattern over a given airfoil depends strongly on airfoil geometry, Reynolds number, Mach number and

angle of attack, etc. But the relationship between the occurrence of a specific flow regime and the above-mentioned factors is far from being clarified. This complexity may lead to a result that different turbulence models may give qualitatively distinct predictions for a separated flow [28]. For example, in our computation of flow around a NACA0015 airfoil at some poststall angles with high Reynolds number, the SA and k-ε models produce a steady-state flow with a stationary separation bubble being present over the airfoil, rather than a physically reasonable unsteady turbulent flow with quasiperiodic vortex shedding. The k-ω SST and RSM models, however, can qualitatively resolve the unsteady flow, though there may be difference between them in the predicted flow structures.

Nevertheless, a problem encountered in the k-ω SST model simulation is that the predicted free shear layer, especially at high Reynolds number, is fairly stable and not receptive to plasma-discharge induced disturbance. In other words, the shear layer is perturbed by disturbance slightly only, but cannot be destroyed fully to produce a reattached flow. On the contrary, the plasma actuation process can be successfully resolved by RSM model, which is employed in this study and briefly described below.

In RSM model, the transport equations for the Reynolds stress $\tau_{ij}^R = -\rho\overline{\upsilon_i'' \upsilon_j''}$ may be written as

$$\frac{\partial}{\partial t}(\rho\overline{\upsilon_i'' \upsilon_j''}) + \frac{\partial}{\partial x_k}(\rho\upsilon_k\overline{\upsilon_i'' \upsilon_j''}) = P_{ij} - \varepsilon_{ij} + \Pi_{ij} + \frac{\partial}{\partial x_k}[D_{ijk} + C_{ijk}], \tag{14}$$

where

$$P_{ij} = -\rho\left(\overline{\upsilon_i'' \upsilon_k''}\frac{\partial \upsilon_j}{\partial x_k} + \overline{\upsilon_j'' \upsilon_k''}\frac{\partial \upsilon_i}{\partial x_k}\right), \quad \varepsilon_{ij} = 2\mu\overline{\frac{\partial \upsilon_i''}{\partial x_k}\frac{\partial \upsilon_j''}{\partial x_k}}, \quad D_{ijk} = \mu\frac{\partial}{\partial x_k}(\overline{\upsilon_i'' \upsilon_j''}),$$

$$\Pi_{ij} = \overline{p\left(\frac{\partial \upsilon_i''}{\partial x_j} + \frac{\partial \upsilon_j''}{\partial x_i}\right)}, \quad C_{ijk} = -\rho\overline{\upsilon_i'' \upsilon_j'' \upsilon_k''} - \overline{p(\delta_{kj}\upsilon_i'' + \delta_{ik}\upsilon_j'')}. \tag{15}$$

In Eq. (14), P_{ij} and $\partial D_{ijk}/\partial x_k$ do not need any modeling. However, ε_{ij}, Π_{ij}, and $\partial C_{ijk}/\partial x_k$ have to be modeled appropriately to close the equations.

The dissipation tensor, ε_{ij}, is modeled as

$$\varepsilon_{ij} = \frac{2}{3}\delta_{ij}\left(\rho\varepsilon + 2\rho\varepsilon\frac{k}{a^2}\right), \tag{16}$$

where $a = \sqrt{\gamma RT}$ is the sound speed.

The scalar dissipation rate, ε, is governed by a transport equation,

$$\frac{\partial}{\partial t}(\rho\varepsilon) + \frac{\partial}{\partial x_i}(\rho\varepsilon\upsilon_i) = \frac{\partial}{\partial x_j}\left(\mu_{\text{eff}}\frac{\partial \varepsilon}{\partial x_j}\right)\frac{1}{2}C_{\varepsilon 1}P_{ii}\frac{\varepsilon}{k} - C_{\varepsilon 2}\rho\frac{\varepsilon^2}{k}, \tag{17}$$

where $C_{\varepsilon 1} = 1.44$, $C_{\varepsilon 2} = 1.92$; $\mu_{\text{eff}} = \mu + \mu_t$ is the total viscosity with the turbulent viscosity computed as $\mu_t = \rho C_\mu k^2/\varepsilon$ where $C_\mu = 0.09$.

The pressure-strain term Π_{ij} is modeled using the method by Launder *et al.* [29]. In fact, both Π_{ij} and $\partial C_{ijk}/\partial x_k$ are finally represented as empirical functions of the mean velocities and Reynolds stresses and their derivatives. The reader is referred to the paper by Launder *et al.* [29] and also the book by Wilcox [30], which details the various approximations and modeling of the turbulence quantities on RHS of Eq. (14). The user guides for OpenFoam and Fluent are also recommended [31,32].

Thus, for a 2D flow, besides the Reynolds averaged Navier-Stokes equations (13), the additional transport equations for Reynolds stress in Eq. (14) and an transport equation for scalar dissipation rate (17) need to be solved.

In this work, Reynolds stress model, which may be the most elaborate RANS turbulence model, is chosen in calculation below under considerations: (i) The model is able to qualitatively predict different flow regimes over airfoil with varying angle of attack and Reynolds number for baseline

TABLE I. Employed parameters in simulation and experiment for poststall flows around a NACA0015 airfoil at different Reynolds numbers. For baseline flows without plasma control, U_p, f, f^+ should be neglected.

Case ID	c (cm)	AoA (deg)	U_∞ (m/s)	Re	U_p (kV)	f (kHz)	$f^+ (=fc/U_\infty)$
A	8	15	10	0.05×10^6	20	0.15	1.2
B	8	15	30	0.15×10^6	20	1	2.67
C	20.32	20	93	1.20×10^6	20	1.25	2.73

flow without actuation. (ii) The unsteadiness of shear layer and its receptivity to plasma disturbance can be well resolved and flow reattachment can be properly reproduced. (iii) The numerical results are overall in good agreement with experiment for both uncontrolled and controlled flows.

3. Numerics

The system of partial differential equations (13) is cast in conservation form and then integrated on a structured quadrilateral mesh using a cell-centered finite volume method. The convective terms of governing equations are discretized using a second-order upwind scheme, whereas time-marching is dealt with using a dual-time-stepping strategy for unsteady calculation. A multigrid technique is used to enhance the convergence of a solution.

4. Resolution of multiscale flow features

The solution strategy is based on the loose coupling of plasma model (1) with RANS equations (13). The system (1) is solved only once to predict the discharge properties. The gas heating effect due to discharge is incorporated into the simulation of external flow, while the influence of mean flow on discharge is considered to be less important and neglected. The plasma-assisted flow control is essentially a multiscale problem with different flow features at disparate time scales which have to be resolved appropriately. For example, for Case A in Table I, the characteristic time of mean flow around airfoil, c/U_∞, is a factor of approximately 23000 larger than time scale of heating, 350 ns. In addition, the shock wave decays to an acoustic-wave-like perturbation tens of microseconds after discharge, while relaxation of residual heat to the ambient condition takes longer than the shock dissipation. Therefore, an adaptive time step method is employed to correctly resolve these flow features and reduce computational cost. For instance, in each actuation period, the initial time step Δt must be small enough to resolve the gas heating process. Then the value of Δt is increased to efficiently capture shock propagation and convection of residual heat and finally increased to a maximum after the residual temperature relaxes to the ambient temperature. It should be guaranteed that the obtained solution is largely independent of time step sizes.

III. EXPERIMENTAL SETUP

A. Wind-tunnel facility and airfoil model

In the present study, experiment is conducted for low Reynolds number flows at $\mathrm{Re} = (0.05, 0.15) \times 10^6$. The PIV visualization of transient flow and measurement of aerodynamic force on airfoil model are performed in a low-speed, open-loop, blown-down-type wind tunnel at Temasek Laboratories of National University of Singapore. The wind tunnel, whose photograph is presented in Fig. 5(a), has a contraction ratio of 9.8 and a square test section of 0.16 m × 0.16 m with test section length of 0.75 m. The maximum working flow speed is 30 m/s, and the turbulence intensity is less than 0.25%. The used NACA0015 airfoil model shown in Fig. 5(b) is made of nylon and has a chord length of 8 cm and a span of 15.8 cm. The DBD actuator is composed of a dielectric layer made of four layers of Kapton films and two copper foil electrodes mounted on both sides of the former. The airfoil model with 0.7 mm recessed design on its front part allows the actuator to be

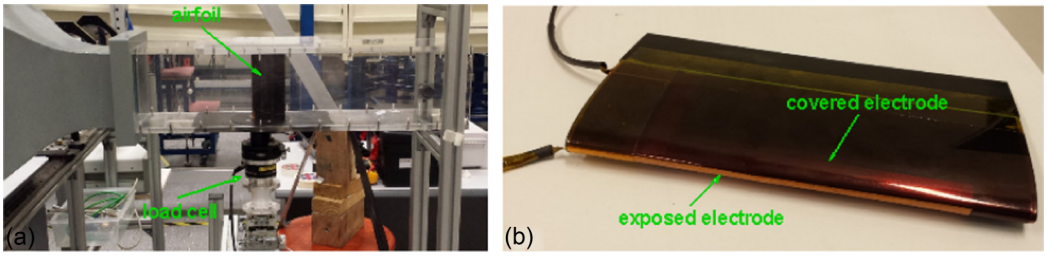

FIG. 5. Experimental setup in wind tunnel (a) and NACA0015 airfoil model (b).

flushed mounted [Fig. 5(b)]. A NPG-18/3500 pulse generator is used, which can nominally provide repetitive voltage pulse signals with peak voltage from 12 to 20 kV at matched 75 Ohm load, pulse rise time about 4 ns, repetition rate up to 3.5 kHz, and pulse energy up to 30 mJ/pulse.

Due to the limitation of wind tunnel, here only low Re flows are investigated experimentally with results presented in Sec. IV B. The nominal working flow speeds are 10 and 30 m/s, which together with chord length of 8 cm produce Reynolds numbers of $\mathrm{Re} = (0.05, 0.15) \times 10^6$, respectively. The experimental data for high Re flow without PIV images are obtained from the literature.

B. Aerodynamic force measurement

For the measurement of lift and drag forces on airfoil, an ATI Gamma piezoelectric gauge is used with the setup of load cell measurement shown in Fig. 5(a). The transient velocity field is acquired using a two-velocity-component dynamic PIV system (LaVision). A Nd:YLF PIV laser is used to generate a pair of thin light sheets. The maximum power can be as high as 30 mJ for each pulse at repeating rate of 1 kHz, and the power used in the current experiment is around 12 mJ. The time between two image frames used for particle scattering is set according to flow velocity, camera magnification, and subregion area for cross-correlation. Two images with interval time $\Delta t = 20\,\mu$s are taken using a Phantom Miro 320s high-speed camera of 1920 × 1200 pixel equipped with a Nikkor 105 mm f1:2.8D lens. For each image, 32 × 32 pixels of subregion area with 50% overlap are adopted in performing the cross-correlation. An aerosol generator [Dantec high-volume liquid seeding generator (10F03)] is used to provide oil-based particles of mean diameter of 1–3 μm. The PIV data are sampled at a frequency of 693 Hz. The nanosecond pulse generator and PIV system are synchronized by a DG645 digital delay generator.

C. Electrical measurement

Pulse voltage and current are measured using a high-voltage probe (Tektronix P6015A) and a current shunt probe (Megaimpulse CS-10/500), respectively. The current probe has an internal impedance of 0.2Ω and a time resolution of 1 ns. Figure 6(a) shows the measured voltage and current traces for the actuator mounted on airfoil leading edge shown in Fig. 5(b). The peak voltage and current are approximately 24 kV and 215 A, respectively. The corresponding instantaneous power and time-resolved energy coupled to the actuator are depicted in Fig. 6(b). The steady-state energy, which is reached around 50 ns after the initiation of pulse, is about 15 mJ. The resulting total coupled energy per unit actuator length in the spanwise direction is approximately $\widehat{\mathbf{Q}}_{\mathrm{couple,\,exp}} = 1$ mJ/cm. This experimental value is smaller than the prediction of $\widehat{\mathbf{Q}}_{\mathrm{couple}} = 1.1$ mJ/cm by plasma model (1) for $U_p = 20$ kV with $\tau_r = 10$ ns. However, this is not a major factor that may lead to the possible discrepancy between simulation and experiment, if any, in the flow control presented later.

Our simulation indicates that the plasma control is effective only if the applied pulse voltage amplitude exceeds a certain threshold value. Usually, for a given airfoil geometry, the higher the Reynolds number, the larger the threshold voltage. Above this critical value, the control authority is not very sensitive to the voltage amplitude. An example is that the difference in the predicted lift and drag on airfoil between 20 and 30 kV is not remarkable for Case B in Table I; refer to Fig. 7. In

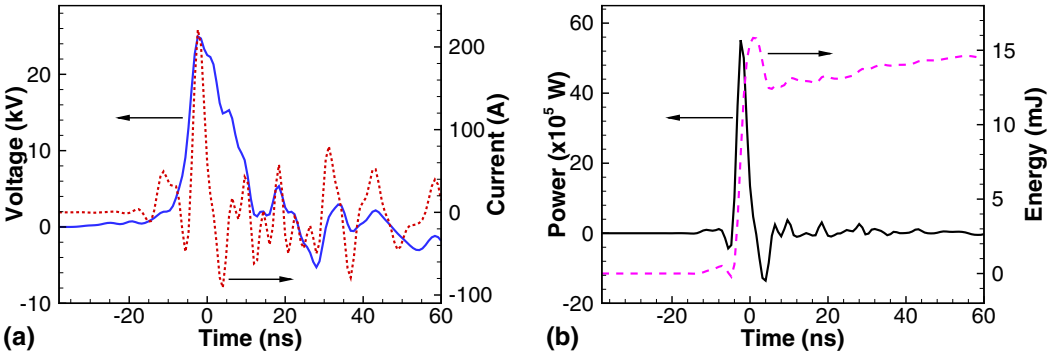

FIG. 6. Voltage and current waveforms (a) and instantaneous power and coupled energy traces (b) measured in experiment.

this study, the nominal pulse voltage in experiment and simulation, $U_p = 20\,\text{kV}$, is high enough to suppress the flow separation around airfoil at Reynolds numbers considered here.

IV. RESULTS AND DISCUSSION

A. General remarks on simulation and experiment

In this study, flow separation control over a NACA0015 airfoil with freestream condition of $p_\infty = 10^5$ Pa and $T_\infty = 300$ K is investigated for three chord Reynolds numbers, $\text{Re} = (0.05, 0.15, 1.2) \times 10^6$. Low Re flows at $\text{Re} = 0.05 \times 10^6 (10\,\text{m/s})$ and $0.15 \times 10^6 (30\,\text{m/s})$ which are based on chord length of $c = 8\,\text{cm}$ are studied both experimentally and numerically. Simulation is performed for high Re flow at $\text{Re} = 1.2 \times 10^6 (93\,\text{m/s}, \text{c} = 20.32\,\text{cm})$ to reproduce the experiment by Rethmel *et al.* [9]. Flow parameters for three typical cases are summarized in Table I. As freestream Mach number considered here is less than 0.3, flow is close to incompressible regime. Hence, the Reynolds number is the main similarity parameter, and the choice of chord length c does not affect our result analysis. Unless otherwise stated, all the flows studied below are assumed to be turbulent with RSM turbulence model employed in simulation. Animation from experiment is provided as Supplemental Material for Case A in Table I [33]. Also shown is the Supplemental Material from simulation for Case C [33].

To make the paper more concise, the validation of plasma model in quiescent air is presented in Appendix 1, while grid convergence study for airfoil flow simulation is given in Appendix 2.

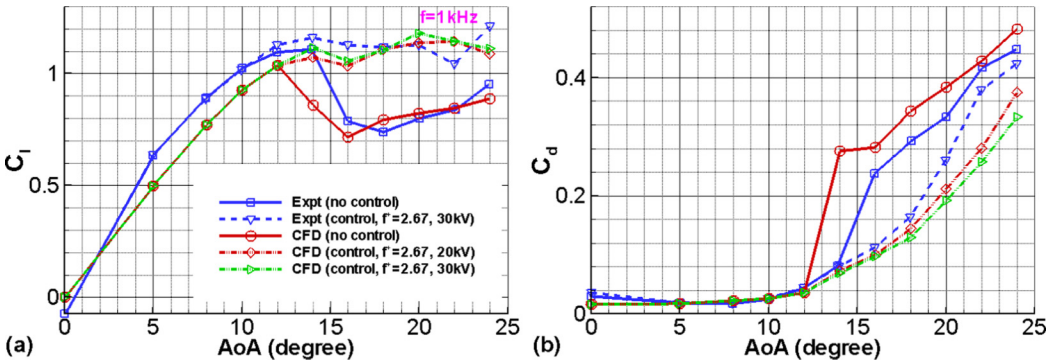

FIG. 7. Comparison between experiment and simulation for lift and drag coefficient as a function of angle of attack for both uncontrolled and controlled flows at $\text{Re} = 0.15 \times 10^6$ ($U_\infty = 30\,\text{m/s}$).

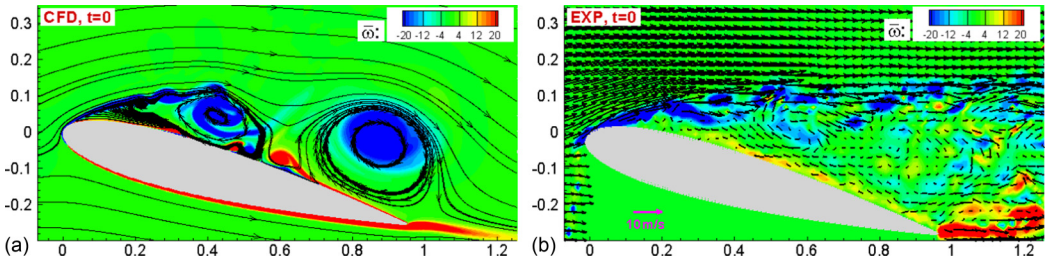

FIG. 8. Comparison between simulation (a) and experiment (b) for transient flow field of baseline flow without control at Re $= 0.05 \times 10^6$ (10 m/s) and AoA $= 15^o$. The normalized vorticity is given by $\overline{\omega} = \omega c / U_\infty$. The instantaneous velocity field in experimental image (b) is obtained with dynamic PIV system. Plasma control is to be applied to the flows shown in the two images where time is reset to 0. Unless otherwise stated, in all the contour plots of this paper, x and y axis variables are x/c and y/c, respectively.

B. Flows at low Reynolds numbers of (0.05, 0.15) × 10^6

1. Baseline flows without control

To investigate flow reattachment process due to nanosecond discharge and reveal two possible control mechanisms, flows at two low Reynolds numbers of Re $= 0.05 \times 10^6$ (10 m/s) and 0.15×10^6 (30 m/s) are studied numerically and experimentally. Experimental data, especially PIV measurement of transient velocity field, are obtained. Experiment is compared with and complemented by simulation. Flow parameters for two low Re cases at AoA $= 15^o$ are listed in Table I.

a. Overview of baseline flows. We start with the documentation of aerodynamic characteristics of airfoil in baseline flow without actuation at Re $= 0.15 \times 10^6$ (30 m/s). Simulation is carried out using an O-type structured mesh of 750 × 250 (circumferential × normal) for which grid independence has been checked. No-slip and far-field boundary conditions are imposed on airfoil surface and outer boundary located around $20c$ away from the surface of airfoil, respectively. The value of y^+ in the first layer of grid adjacent to airfoil surface is maintained at around 1. In Appendix 1, a grid convergence study is presented for the high Re case. Figure 7 shows the measured and predicted lift and drag coefficient as a function of angle of attack in the range $0 \leqslant \text{AoA} \leqslant 24^o$. The calculated lift and drag curves are seen to concur well with their experimental counterparts (Fig. 7). The predicted stall angle of 12^o is close to experimental measurement of 14^o. Aerodynamic force on airfoil at low Re of 0.05×10^6 (10 m/s) is relatively small and not measured in experiment.

Figures 8 and 9 depict the comparison of calculated transient flow field and that measured with PIV for baseline flows at two Reynolds numbers. Airfoil is placed at poststall angle of AoA $= 15^o$. It is seen from Figs. 8 and 9 that predicted transient flow pattern is qualitatively similar to the PIV flow visualization result in terms of topology of separated shear layer as well as structures

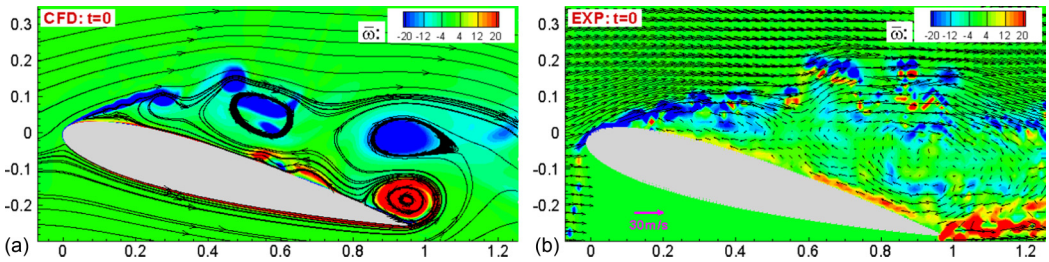

FIG. 9. Comparison between simulation (a) and experiment (b) for transient flow field of baseline flow at Re $= 0.15 \times 10^6$ (30 m/s) and AoA $= 15^o$.

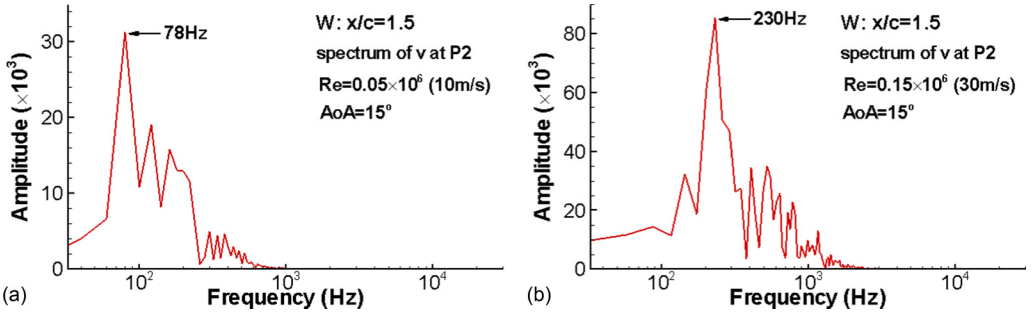

FIG. 10. Predicted spectra of y velocity at characteristic location P_2 on wake monitoring line $x/c = 1.5$ as sketched in Fig. 2 for the baseline flows at Re $= 0.05 \times 10^6$ (10 m/s), AoA $= 15^o$ (a) and Re $= 0.15 \times 10^6$ (30 m/s), AoA $= 15^o$ (b).

of individual vortices in large separation region and trailing edge vortex. The slight discrepancy between simulation and experiment is that the RANS calculation produces a bit more organized flow pattern with smoother streamlines. Actually, the 2D RANS modeling cannot faithfully resolve the complex poststall airfoil flow as such flow around a large aspect ratio or 2D wing is essentially 3D. Although the spanwise fluctuation can be resolved by 2D Reynolds-averaged approach, small eddies in the perturbed shear layer may not be modeled properly [28]. However, as discussed above and will be seen later, our 2D RANS simulation produces good agreement with experiment in terms of both the qualitative flow features and the quantitative statistics of the solution. Meanwhile, the appropriateness of use of the RANS model is further supported by the observation made in the simulation of airfoil flow control presented below that the boundary layer near the actuator is thin with respect to the actuator scale. It is thus believed that our numerical results with acceptable level of accuracy will give some insights into the understanding of physics and mechanism of poststall flow and its control.

b. Spectrum analysis. In a control system, a key parameter is the forcing frequency f, which is usually scaled with chord length and freestream speed to form a dimensionless reduced frequency, $f^+ = fc/U_\infty$, for which other definitions also exist. For a specific airfoil flow, the optimum f^+, which is usually identified based on lift enhancement, is conjectured to be related to both local shear layer instability and global instability that causes trailing edge vortex shedding, though such a relation has not been established. Each of the instabilities is characterized by a natural frequency. Therefore, the prediction of characteristic frequencies of these two basic flow constituents, shear layer and trailing edge vortex, will provide some guidance to our calculation.

Here spectral analysis of y velocity is conducted for characteristic location, P_2, in the wake through simulation. As sketched in Fig. 2, vertical line W is located in the wake with $x/c = 1.5$, and the location, P_2, corresponds to the maximum root mean square (rms) velocity. Spectral curves are plotted in Figs. 10(a) and 10(b) for baseline flows at Re $= 0.05 \times 10^6$ (10 m/s) and 0.15×10^6 (30 m/s), respectively. For Re $= 0.05 \times 10^6$, the predicted peak frequency is $f_{\text{shed}} = 77$ Hz ($f^+_{\text{shed}} = 0.62$), whereas for Re $= 0.15 \times 10^6$, the predicted peak frequency of 230 Hz ($f^+_{\text{shed}} = 0.61$) is very close to the experimental measurement of 225 Hz. Meanwhile, in Ref. [28], characteristic frequency of a shear layer like that at P_1 sketched in Fig. 2 is found to satisfy $f_{\text{shear}}/f_{\text{shed}} = \mathcal{O}(10)$.

2. Flow control at two low Reynolds numbers

Next, plasma control will be applied to the baseline flows depicted in Figs. 8 and 9 for two Reynolds numbers. Refer to Cases A and B in Table I for employed parameters. Actuation period is defined as $T_p = 1/f$ with f being pulse frequency. Figure 5(b) shows the photograph of the airfoil model with actuator. Consistent with experiment, in the numerical setup, the actuator is placed on

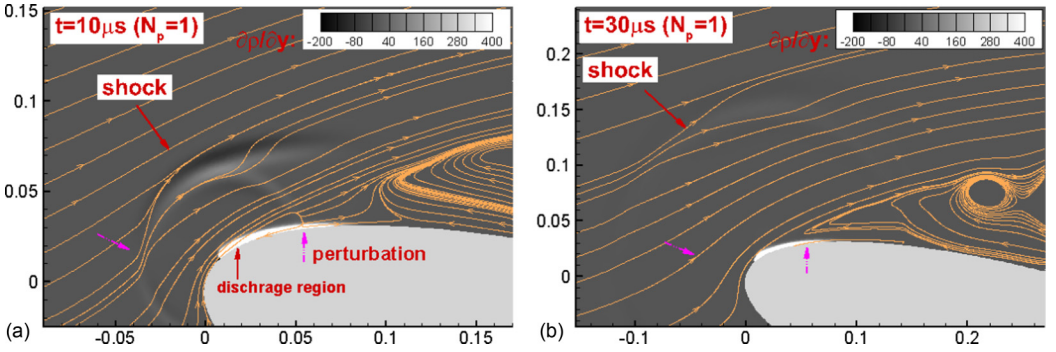

FIG. 11. Numerical Schlieren images overlaid with streamlines showing the propagation of shock wave through external flow due to the first pulse discharge. The flow is under plasma control with parameters, $\mathrm{Re} = 0.05 \times 10^6$ (10 m/s), AoA $= 15^o$, $U_p = 20$ kV, $f = 0.15$ kHz, $f^+ = 1.2$ (Case A in Table I). In each plot, N_p denotes the number of voltage pulses which have been discharged. Scalings of x and y axis are different in two images for a clear reading.

the leading edge of airfoil as sketched in Fig. 3(b). Time is measured from the implementation of the first pulse.

Before embarking upon the detailed description of results, let us first discuss limitations of experiment and simulation. As sampling frequency of PIV (693 Hz) is not very high, shock evolution arising from a discharge cannot be well captured. Another problem is that the boundary layer over airfoil surface cannot be accurately resolved by PIV measurement as there are simply insufficient particles to define the detailed flow field near surface. The major limitation of our simulation lies in the incapability of the RANS model to predict laminar-to-turbulent transition of shear layer. However, as will be seen later, the use of the RANS model with full turbulent flow assumption is, we reckoned, not a drawback of this study and instead is enough to resolve the control process of most poststall flows where the control mechanism relies on the excitation of inherent flow instability (and transition to turbulence does not take a major role).

a. Impact of shock wave on flow. Low Re flow at $\mathrm{Re} = 0.05 \times 10^6$ (10 m/s) is examined first. Actuator is driven by repetitive pulses with $U_p = 20$ kV, $f = 0.15$ kHz (Cases A in Table I). To gain some insights into the role of shock wave in flow control, the shock propagation through flow after the first pulse discharge is visualized in Fig. 11, where numerical Schlieren images are overlaid with streamlines. Recall that the shock propagation through quiescent air introduces perturbation to flow properties in a narrow region behind the shock front, and meanwhile the shock decays very fast (see Appendix 1 and Figs. 25 and 26 for the behavior of discharge-induced shock in quiescent air). In the current case with the presence of an existing velocity field, the shock-induced perturbation manifests its existence as distortion of streamlines across shock front, as seen in the Schlieren image at $t = 10\,\mu$s in Fig. 11(a), where the shock wave has moved a short distance away from the discharge region and streamlines across shock front are deformed appreciably. Apparently, at a given time, the resulting disturbed flow pattern depends on both background flow speed and shock intensity. With the rapid shock decay, by $t = 30\,\mu$s, the streamlines are distorted slightly only [Fig. 11(b)]. Because of the highly transient nature of shock-produced perturbation, the state of the flow region swept by shock wave, such as that marked by pink arrow in Fig. 11(a), has returned to close to its undisturbed state. After $t = 50\,\mu$s, the flow (not shown here) does not appear to be disturbed by shock wave any more. The implication here is that although the rapid shock propagation can introduce transient perturbation in the vicinity of the shock front, it does not cause any lasting alterations to flow structure. It thus can be concluded that shock passage through flow contributes little to flow control once the shock travels outside the discharge region.

b. Impact of residual heat. However, with time moving on, a significant change in flow field is found to have occurred, as illustrated in Fig. 12, where a normalized temperature field with

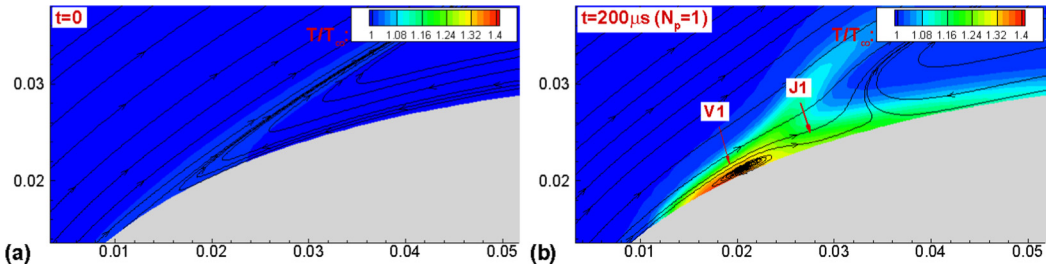

FIG. 12. Generation of spanwise vortices due to the first pulse discharge, $\mathrm{Re} = 0.05 \times 10^6$ (10 m/s), $\mathrm{AoA} = 15^o$, $f^+ = 1.2$ (Case A in Table I). Temperature is normalized by freestream value $T_\infty = 300$ K.

streamlines is depicted. At around $t = 150\,\mu$s, the residual heat due to the first pulse discharge has been advected into the separation region and clockwise-rotating vortices labeled $V1$ have formed near the original separation point of boundary layer; refer to Figs. 12(a) and 12(b). The formation of vortices $V1$ appears to be attributed to the residual heat. The energy deposition in flow during plasma discharge results in a change in the temperature (also in the density and viscosity). The resulting thermal perturbation, i.e., the gradient of flow properties like the temperature, may excite inherent instability of flow, such as Kelvin-Helmholtz instability of the shear layer and eventually induce the generation of vortices. Again, the shock propagation through the discharge volume makes little contribution to the generation of vortices as when the vortices are initiated at $t = 150\,\mu$s, the perturbation caused by shock has decayed already. In Sec. IV D 1, a pure temperature disturbance (without pressure gradient and subsequent generation of shock wave) is also found to be able to produce similar spanwise vortices. These results indicate that the thermal perturbation (regardless of whether it is density or viscosity based disturbance) [8] has the greatest contribution to vortices generation. These vortices entrain external fluid with high momentum into the flow separation region over the suction surface, resulting in a flow jet labeled $J1$ in Fig. 12(b). The induced vortices $V1$ closely follow the advection of residual heat by the external flow, move downstream, grow in size, and intensify in strength. By the end of the first actuation period, $t = 6.67$ ms $= 1T_p$, the residual temperature has relaxed to ambient condition. Next, the second pulse is implemented. Again, new vortices $V2$ form near the discharge region shortly after the second pulse, as shown in Fig. 14. The initiation of spanwise vortices in the vicinity of boundary layer and their early stage growth cannot be captured by PIV. In fact, the principal flow feature associated with each pulse discharge is the generation of spanwise vortices together with a flow jet, which seem to be induced by residual heat rather than shock wave.

c. Flow reattachment. The process of flow reattachment is summarized in Fig. 13 where the left column shows a sequence of vorticity contour images from simulation, whereas the corresponding sequence of experimental PIV velocity field images is presented in the right column for a comparison. Pleasingly, the simulation and experiment produce almost the same salient features of shear layer breakup under the impact of a few pulse discharges. Figure 13(a) depicts the computed flow field $0.65T_p$ after the first pulse is discharged, from which it is seen that the shear layer has broken up from the leading edge of airfoil and the original separation region has shrunk under the impact of jet $J1$. The predicted flow pattern and structures like spanwise vortices $V1$ and jet $J1$ resemble their experimental counterparts shown in Fig. 13(b). By $t = 1.5T_p$, the separation region has been pushed to move further downstream. Vortices $V1$ roll off the airfoil leading edge under the impact of jet $J2$ arising from the second pulse and merge into a single vortex as they move downstream. This procedure is illustrated in Fig. 14. Again, as shown in Figs. 13(c) and 13(d), numerical and experimental results agree well with each other except that jet $J1$ in simulation appears to move faster. Actually, with the implementation of more pulses, the procedure similar to that in Fig. 14 occurs repeatedly, and vortices $V2$, $V3$, and $V4$ are seen to move downstream along the suction surface one after another; refer to Figs. 13(e)–13(h). In other words, each pulse generates a spanwise

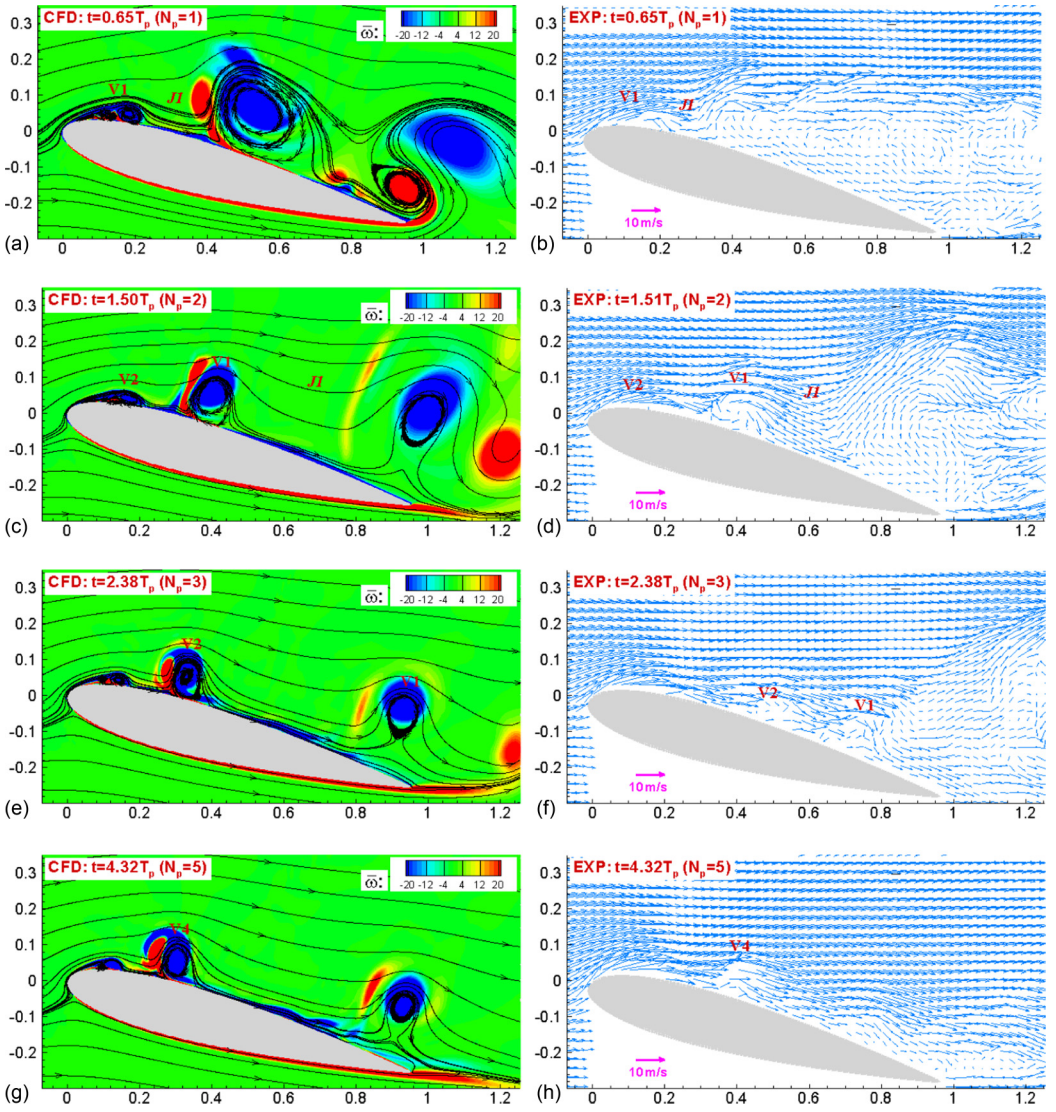

FIG. 13. Numerical (left column) and experimental (right column) images show flow reattachment under the impact of a few pulse discharges for $\mathrm{Re} = 0.05 \times 10^6$ (10 m/s) (Case A in Table I). The transient velocity fields in the right column are measured using dynamic PIV system.

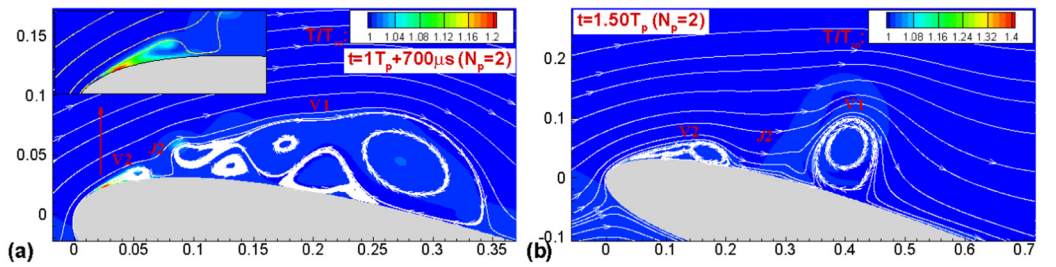

FIG. 14. Advection of residual heat due to the second pulse, $\mathrm{Re} = 0.05 \times 10^6$ (10 m/s).

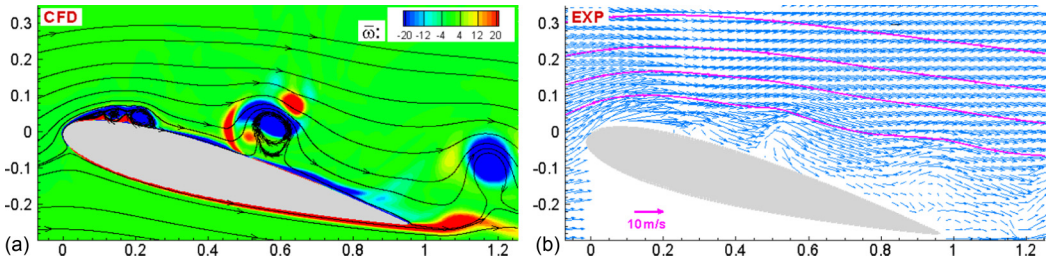

FIG. 15. Transient flow fields of controlled flow from simulation (left) and experiment (right), Re = 0.05×10^6 (10 m/s).

vortex. Meanwhile, the separated shear layer completely breaks down and is finally forced to shed off in both simulation and experiment [Figs. 13(e)–13(h)]. After about 10 pulses, the flow has been fully controlled and evolved into a new quasiperiodic state. The typical transient flow fields from simulation and experiment in this regime are compared in Fig. 15. Both numerical and experimental images of Fig. 15 show that the completely controlled flow is characterized by a partially reattached flow with a train of downstream moving vortices. A slight discrepancy between them is that a separation region such as that shown in Fig. 15(a) is always present near the leading edge in numerical result. This region varies in size with time but cannot be suppressed. However, this flow structure is not apparent in the experimental image. The leading edge region shown in Fig. 15(b) is empty of particles. But this may also indicate the possible presence of separation, which prevents particles used in PIV being seeded into the separation region.

For a comparison, the effectively controlled flow at Re = 0.15×10^6 (30 m/s) is illustrated in Fig. 16. Repetitive pulses with voltage of $U_p = 20$ kV and frequency of $f = 1$ kHz are used (Cases B in Table I). Simulation and experiment show nearly the same flow reattachment process, which is similar to that in the previous low Re case and not shown here to save space. Again, spanwise vortices associated with multiple discharges make the separated flow being reattached. As reflected in the plot of time history of predicted lift and drag coefficient in Fig. 17(b), the period of cyclic flow variation appears to be consistent with that of actuation and seems to be "locked" by the latter after the forced flow becomes quasiperiodic. However, the difference in controlled flow pattern between simulation and experiment is evident, as shown in Fig. 16. The predicted vortices train over the suction surface is not apparent in the experimental image. PIV measurement of the transient velocity field shows that the flow appears to be fully attached except for that near leading and trailing edges. This may be attributed to the control mechanism, which is different from that of the previous low Re case.

d. Discussion of control mechanism. The question raised here is, What is the flow control mechanism and what leads to the different forced flow patterns at two low Reynolds numbers in

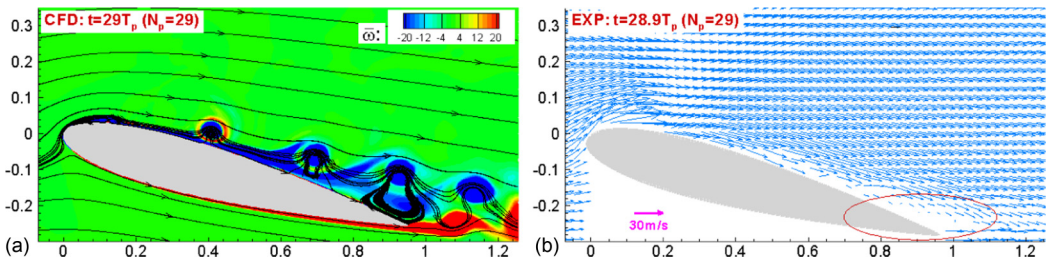

FIG. 16. Transient flow fields of controlled flow from simulation (left) and experiment (right), Re = 0.15×10^6 (30 m/s), AoA = 15°, $U_p = 20$ kV, $f^+ = 2.67$ (Case B in Table I).

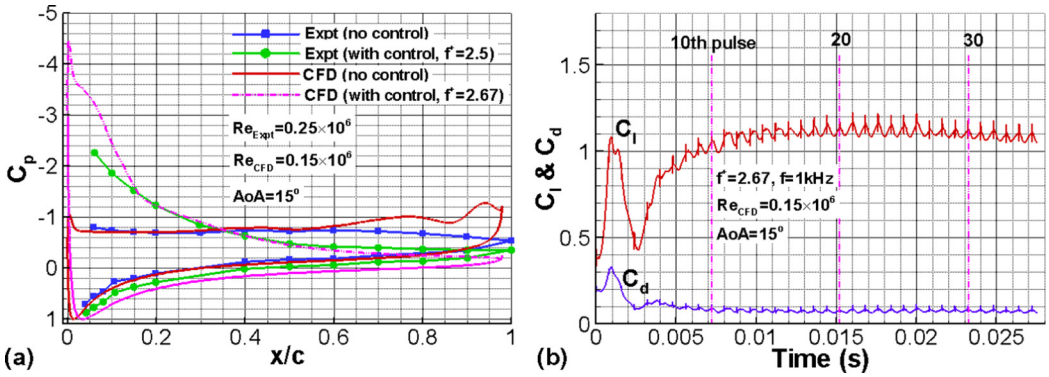

FIG. 17. The comparison of pressure coefficient distributions along airfoil surface between experiment and simulation for both uncontrolled and controlled flows (a) and time histories of predicted lift and drag coefficients with plasma control (b) for $\mathrm{Re} = 0.15 \times 10^6$ (30 m/s). In plot (a), the measurement associated with $\mathrm{Re} = 0.25 \times 10^6$ from Ref. [9] is plotted.

experiment [Figs. 15(b) and 16(b)]? It seems that there may be two distinct nanosecond actuation mechanisms: excitation of flow instability and active trip. At low $\mathrm{Re} = 0.05 \times 10^6$ (10 m/s) and $\mathrm{AoA} = 15^\mathrm{o}$, the nanosecond actuator is believed to trigger flow instability, producing large-scale coherent spanwise vortices, which result in and further maintain flow reattachment (Fig. 15). This is confirmed by both simulation and experiment. However, when Re is increased to $\mathrm{Re} = 0.15 \times 10^6$ (30 m/s) (with AoA fixed at 15^o), the actuator may function in a different way. Although the preliminary flow reattachment is still realized by exciting shear layer instability and producing spanwise vortices, the attachment state may be sustained by accelerating laminar-to-turbulent transition of shear layer near the leading edge and generating an attached turbulent boundary layer over the suction surface (Fig. 16). In other words, the nanosecond actuator may perform as an active trip in the quasiperiodic regime. But this cannot be confirmed by simulation as the RANS model cannot predict the transition process. The incapability of the RANS approach to predict transition process may lead to the discrepancy between simulation and experiment shown in Fig. 16. It is hypothesized in Refs. [9,10] that for a specific airfoil flow control, the first mechanism, i.e., excitation of flow instability, plays a dominant role in the poststall regime, while at attack angle near stall, the second mechanism, active trip, plays a major role. In the current case, the increase of Re from 0.05×10^6 to 0.15×10^6 leads to change in stall angle. Therefore, the control mechanisms and resulting flow patterns may be different at the same attack angle for two Reynolds numbers. The conclusion is that regardless of what values of Re and AoA are, the initial reattachment of the separated shear layer is achieved by triggering flow instability. The residual heat-induced spanwise vortices bring external flow with high momentum to separation region. After that, for a given Re, at a wide range of poststall AoA (usually $\mathrm{AoA} > \alpha_{\mathrm{stall}} + 2^\mathrm{o}$ with α_{stall} being stall angle), nanosecond actuator continues providing perturbations and generating spanwise vortices, resulting in a partially reattached flow with a train of repetitive, downstream moving vortices. (For instance, experiment shows that at $\mathrm{Re} = 0.05 \times 10^6$ (10 m/s), at least for poststall AoA range of $\mathrm{AoA} \geqslant 15^\mathrm{o}$, flow instability excitation is the main control mechanism.) However, at a relatively narrow range of AoA near stall (usually $\alpha_{\mathrm{stall}} \leqslant \mathrm{AoA} \leqslant \alpha_{\mathrm{stall}} + 2^\mathrm{o}$), nanosecond discharge may act as an active trip, producing an attached turbulent boundary layer over airfoil surface.

It should be pointed out that although the current RANS calculation may not well resolve the transient flow under control over a narrow range of angles of attack near stall, it is valid for most poststall flows. Even in the vicinity of stall, this is not expected to affect time-averaged quantities, such as average pressure, lift and drag coefficients, and evaluation of control authority. Our ongoing work is to use LES simulation to further elucidate the boundary layer tripping mechanism behind nanosecond plasma actuation near stall.

e. Control effect. To quantify the control effect, the predicted and measured pressure distributions are compared in Fig. 17(a) for $\mathrm{Re} = 0.15 \times 10^6$ (30 m/s) and $\mathrm{AoA} = 15^\circ$, where the experimental data associated with $\mathrm{Re} = 0.25 \times 10^6$ from Ref. [9] is plotted, as we did not measure airfoil surface pressure. The baseline flow has a flat pressure profile along suction surface with near-zero pressure gradient, a typical feature of massively separated flow. The plasma control, however, recovers a suction peak of about −4.5 in simulation. The observation that the pressure distribution with control is not very smooth before $x/c = 0.15$ and becomes relatively flat past $x/c = 0.75$ is consistent with the presence of leading and trailing edge separation shown in Fig. 16. Moreover, the predicted lift coefficient concurs relatively well with the measurement, and the stall angle is extended to at least 24° [Fig. 7(a)], a remarkable achievement. Meanwhile, another benefit of the control is that the drag is also reduced greatly in both simulation and experiment, as shown in Fig. 7(b). Simulation result shows that over the investigated poststall attack angle range $14^\circ \leqslant \mathrm{AoA} \leqslant 24^\circ$, the average lift coefficient increment and drag coefficient reduction are 0.28 and 0.17, respectively, which correspond to an average 34% increase in lift and an average 50% decrease in drag. By contrast, the experimental average lift increase and drag decrease over $16^\circ \leqslant \mathrm{AoA} \leqslant 24^\circ$ are $\Delta(C_l)_{\mathrm{avg}} = 0.3$ (a 37% increase) and $\Delta(C_d)_{\mathrm{avg}} = 0.078$ (a 27% decrease), respectively.

f. Possible influence of slow heating on flow control. In Sec. II A, it is stated that there is a slow heating process in plasma on a much longer time scale of $\sim 200\,\mu$s, following the fast energy thermalization modeled in our work. Here the possible impact of the second stage gas heating on flow control is examined in Case A. The slow energy thermalization is assumed to occur after the fast heating and is modeled by imparting an additional heating energy $\widehat{\mathbf{Q}}_{\mathrm{slow}}$ to the flow in each actuation period in a similar way as in the earlier fast heating. $\widehat{\mathbf{Q}}_{\mathrm{slow}}$ is arbitrarily set equal to $\widehat{\mathbf{Q}}_{\mathrm{couple}}$ of fast heating as we cannot obtain its accurate value from experimental data in Ref. [27], but is assumed to be converted into gas heating on a longer time of $\tau_{\mathrm{slow}} = 200\,\mu$s. The distinction between the two stages of energy thermalization process is that the slow heating is significantly "softer" than the fast heating as the heating time of the former is two orders of magnitude larger than that of the latter. As a result, the flow perturbation caused by the "softer" heating is much weaker compared with that arising from the fast heating. Our simulation results (not shown here to save space) demonstrate that for the current poststall case, the slow heating has little influence on the flow features and whole flow control process. The spanwise vortices are still induced by the fast heating. Our calculation indicates that, to generate such large-scale vortices, the heating caused perturbation must be intensive enough. Therefore, the slow heating effect is thought to be of secondary importance in poststall flow separation control and can be neglected. However, for flow near stall where the laminar-to-turbulent transition may be the major mechanism for sustaining an attached flow, the effect of slow heating may become pronounced. As stated earlier in Sec. II A, the localized and random perturbations associated with individual filaments due to the later heating may act as an induced surface roughness and promote turbulent transition in the boundary layer. For this, more efforts need to be made towards the improvement of both the experimental and modeling work, which may include the use of large eddy simulation and improvement and calibration of the current plasma model with more experimental data of two-stage heating in plasma discharge.

C. Flow at high Reynolds number of 1.2×10^6

As stated earlier, the nanosecond DBD actuator has demonstrated great potential to control high-speed flow. However, high Re flow slightly differs from low Re case like that studied in the previous subsection, in terms of baseline flow, flow control process, and resulting flow pattern. This motivates us to examine the flow at high Re.

1. Baseline flow without control at $Re = 1.2 \times 10^6$

The present simulation mimics the experiment by Rethmel *et al.* [9], where leading edge separation control on an 8-inch (20.32 cm) chord NACA0015 airfoil is demonstrated for $\mathrm{Re} = 1.2 \times 10^6$ ($U_\infty = 93$ m/s). The predicted mean lift coefficient is compared with experimental measurement

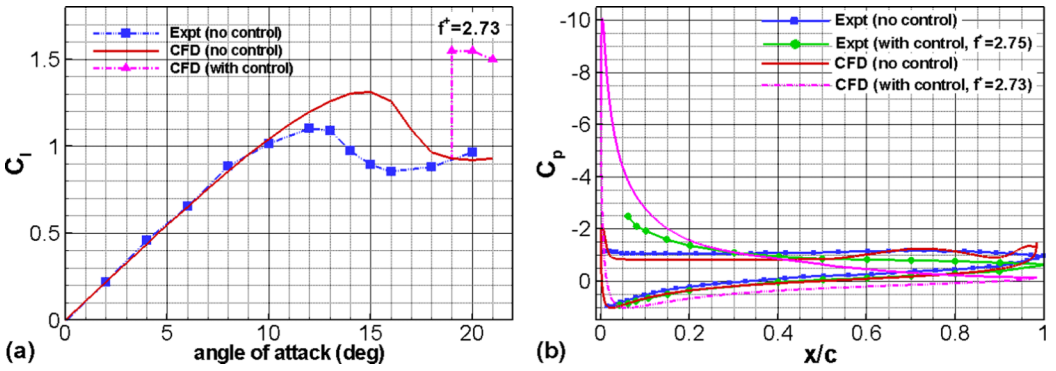

FIG. 18. The comparison between experiment and simulation for time-averaged lift coefficient versus angle of attack (a) and mean pressure coefficient distribution along airfoil surface (b) at Re $= 1.2 \times 10^6$ (93 m/s). In plot (b), AoA $= 20^o$. The experimental data are extracted from Ref. [9].

for $0 \leqslant$ AoA $\leqslant 21^o$ in Fig. 18(a). The snapshot of vorticity field at high poststall attack angle of AoA $= 20^o$ is depicted in Fig. 20(a). In comparison with that at low Re, the current flow is different in two aspects: (i) Flow separation beyond stall and stall itself cannot be predicted accurately. This is attributed to many factors, as discussed in Sec. II B 2. However, as shown in Fig. 18(a), the decreased difference between simulation and measurement in lift coefficient in the deeply stalled regime at AoA $\geqslant 19^o$ implies that the simulated flow may not deviate much from the real case, and this regime happens to be where flow control is to be applied. This is also supported by the good concurrence of calculated and measured pressure distributions along the airfoil surface for AoA $= 20^o$ shown in Fig. 18(b). (ii) In the poststall regime, overall flow pattern and flow structures including shear layer and trailing edge vortex appear to be more regular; see Fig. 20(a). Again, spectral analysis of y velocity is conducted on point P_2 at $x/c = 1.5$ for AoA $= 20^o$ based on simulation. The predicted peak frequency of 279 Hz ($f^+_{\text{shed}} = 0.61$) in the wake yields Strouhal number $S_t = c \sin(\alpha) f_{\text{shed}} / U_\infty = 0.208$ with α being angle of attack. This value is close to the experimental Strouhal number of 0.21 for bluff bodies that include airfoil at a high angle of attack.

2. *Flow control at Re = 1.2 × 10⁶*

Flow control is applied to the deep stall case at AoA $= 20^o$ for which the transient vorticity field is shown in Fig. 20(a). The plasma actuator is mounted near the leading edge of airfoil, as sketched in Fig. 3(a). It is driven by repetitive pulses with $U_p = 20$ kV and $f = 1.25$ kHz, which yields a reduced frequency $f^+ = 2.73$. The forcing frequency $f^+ = 2.73$ is close to the optimum value of $f^+ = 2$ reported in experiment [9]. The values of flow parameters are set according to experiment for a consistent comparison and listed in Case C of Table I. The simulation restarts from the instantaneous solution shown in Fig. 20(a) where time is reset to be 0.

The shock propagation has been shown to have little effect on flow control in the low Re case and therefore is not examined here. The flow actuation process at high Re shares some features with that at low Re. Again, each pulse induces a spanwise vortex. Figure 19 shows that vortex $V1$ is formed 5 μs after the first pulse discharge. Under the impact of successive discharges, the leading edge shear layer is destroyed, as illustrated in Fig. 20 where transient vorticity fields associated with the first 10 pulses are depicted. After this stage, a new quasiperiodic flow pattern is gradually established as reflected in time histories of lift and drag coefficients plotted in Fig. 21. The fully controlled flow features a train of repetitive vortices over the suction surface; see Fig. 22. It is clearly seen that the flow control authority is achieved by triggering flow instability. This is consistent with experimental observation in Ref. [9]. On the other hand, the simulation reveals some characteristics peculiar to the high Re case. First, the high-speed flow appears to be more resilient to the impact of discharges, and the shear layer breakup procedure is more complex; see Fig. 20. Second, after several pulses,

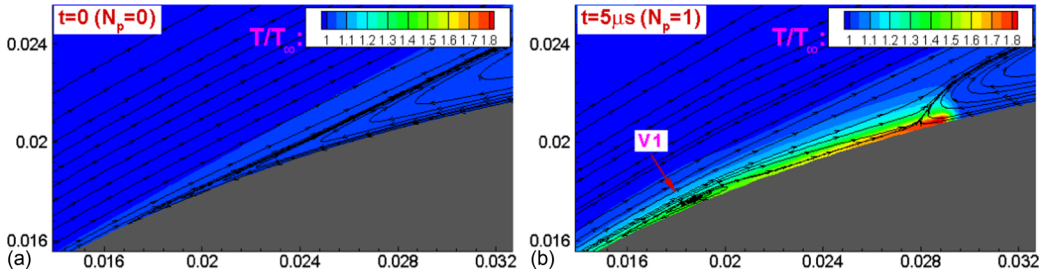

FIG. 19. Advection of residual heat and generation of spanwise vortex due to the first pulse discharge. Here $\mathrm{Re} = 1.2 \times 10^6$ (93 m/s), AoA $= 20^o$, $U_p = 20$ kV, $f^+ = 2.73$ (Case C in Table I).

the separated flow near leading edge is fully attached, and newly induced vortex forms somewhere downstream of discharge region. Figure 23(a) depicts the perturbation caused by the advection of residual heat 80 μs after the 11th pulse discharge, while Fig. 23(b) shows the formation of vortex $V11$. Apparently, vortex $V11$ is generated by a pure thermal perturbation. An interesting finding is that at least from pulse 10, all the new vortices form at approximately the same location $x/c = 0.135$

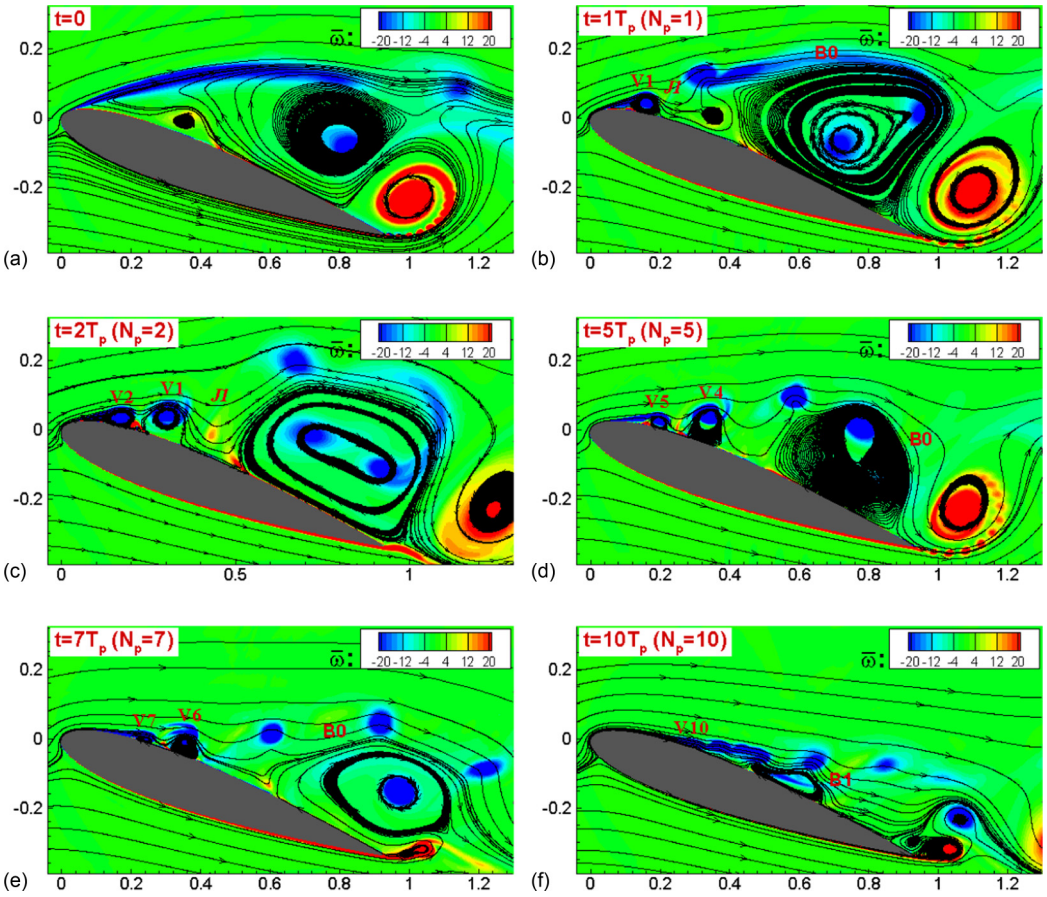

FIG. 20. The breakup of separated shear layer under impact of 10 successive pulses at $\mathrm{Re} = 1.2 \times 10^6$ (93 m/s), AoA $= 20^o$.

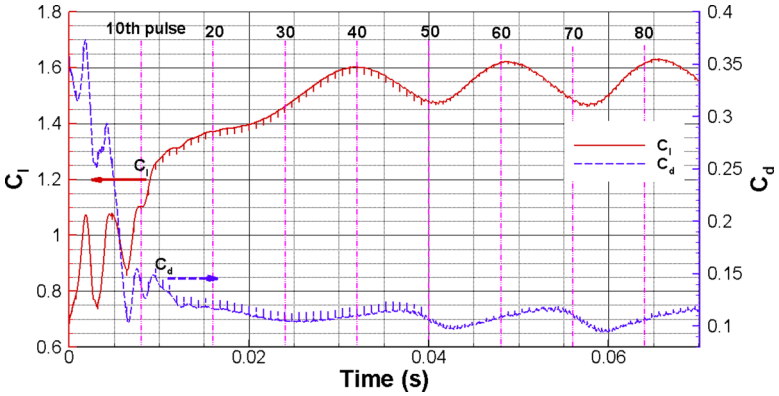

FIG. 21. Time variation of lift and drag coefficients on airfoil with plasma control, Re $= 1.2 \times 10^6$ (93 m/s).

before which the flow has become fully attached. This implies that the nanosecond DBD actuator has a remarkable "moving perturbation source" feature as its influence region can be extended with the advection of residual heat. This flexibility may be the reason that this kind of actuator is more effective and efficient than the traditional one whose influence is restricted to actuator region only. These observations confirm again that the residual heat plays a dominant role in the flow control. Third, as shown in Fig. 21, the variation of controlled flow at high Reynolds number has much longer period in comparison with that of actuation. Finally, in terms of the enhancement of aerodynamic properties, the control authority improves for high Re with larger lift increase obtained; refer to the lift curve and airfoil surface pressure distribution shown in Fig. 18. Due to the lack of experimental data for lift coefficient with plasma control, only the predicted and measured pressure profiles along airfoil surface are compared in Fig. 18(b). The loss of efficacy for AoA $< 19^o$ as shown in Fig. 18(a) is because that the predicted separation point is located somewhere downstream of leading edge and too far from the actuator.

D. Parametric study

1. Impact of pure temperature disturbance

Although in Sec. IV C 2, the residual heat alone is shown to be able to generate vortex after it is advected downstream of the airfoil leading edge [Fig. 23(b)], it is still uncertain whether the nanosecond DBD actuation mechanism arises totally from the thermal effect of residual temperature. To elucidate this, a pure thermal disturbance is considered for the low Re case [Re $= 0.05 \times 10^6$ (10 m/s)] in Sec. IV B 2. Here an instantaneous temperature field is put in the actuator region, which is close to that after a real pulse discharge, while the density is artificially adjusted to guarantee that

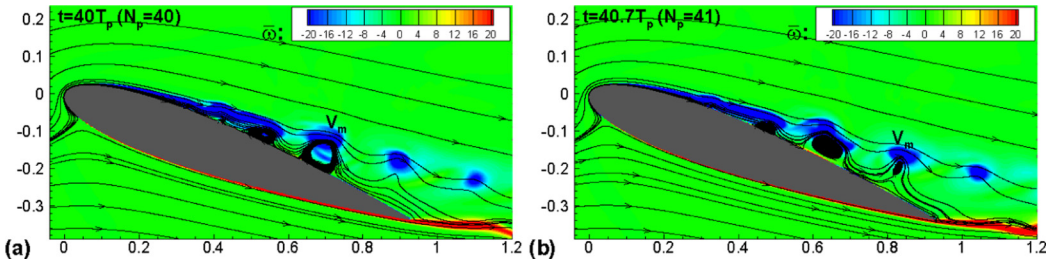

FIG. 22. Transient vorticity field overlaid with streamlines illustrates fully controlled flow at Re $= 1.2 \times 10^6$ (93 m/s), AoA $= 20^o$.

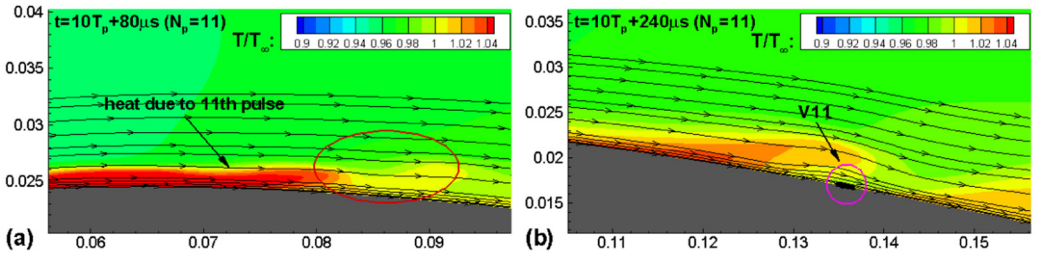

FIG. 23. Perturbation caused by residual heat from 11th pulse (a) and formation of vortex $V11$ induced by residual heat alone (b) for the case shown in Fig. 20.

the pressure remains unchanged and the equation of state, $p = \rho RT$, is still satisfied. In this way, shock wave will not be generated. Figure 24(a) depicts the early stage development of heat induced vortex, which forms about 200 μs after the implementation of pure temperature disturbance. Again, each thermal pulse produces some spanwise vortices, and after about 10 actuation periods with $f^+ = 1.2$, a reattached flow is obtained, as shown in Fig. 24(b), which is comparable to that due to real pulse discharges in Fig. 15(a). However, for the high Re case ($\mathrm{Re} = 1.2 \times 10^6$) in Sec. IV C 2, the vortices train induced by the current multiple pure thermal pulses cannot result in an attached flow comparable to that shown in Fig. 22 from real discharges, though the forced flow (not shown here) is still a notable improvement over the baseline poststall flow. The degradation of control effect with the present pure thermal pulse may be caused by the numerical error introduced by the adjustment of the density field which results in the violation of mass conservation in the whole computation domain. Based on the observations in the two Re cases, the conclusion reached here is that the pure heat disturbance indeed has the potential to trigger flow instability and then control flow and the residual heat from the plasma discharge makes the major contribution to control authority of nanosecond DBD actuator.

However, one has to be cautious about the potential actuation authority of plasma heating in a specific flow system. In Ref. [34], direct numerical simulation is conducted for the control of an axisymmetric Mach 1.3 ideally expanded jet with localized arc filament plasma actuators. It is found that the influence of arc discharge caused intense local heating on the excitation, and control of jet downstream is relatively minor. By contrast, the recessed cavity near nozzle exit, which is designed to shield the plasma from the flow, is essential for the effective flow actuation. It seems that the effectiveness of plasma/thermal heating in controlling a flow relies on a series of factors such as flow Mach number, Reynolds number, presence of separated shear layer, location of heat source, etc. This hopefully can be clarified by improved diagnostics and simulation.

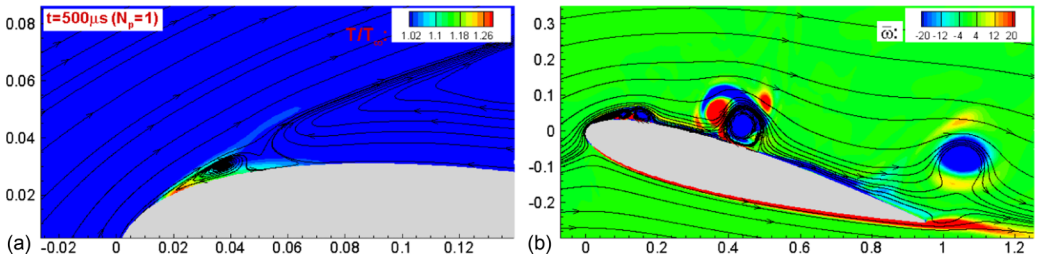

FIG. 24. Flow field associated with pure thermal disturbance at $\mathrm{Re} = 0.05 \times 10^6$ (10 m/s), AoA = 15°. Temperature contour in plot (a) shows the formation of spanwise vortex due to the first thermal pulse, while vorticity contour in plot (b) illustrates the controlled flow pattern.

V. CONCLUSION

The nanosecond plasma actuator-based control of massively separated flows around a NACA0015 airfoil with Reynolds numbers of $\mathrm{Re} = (0.05, 0.15, 1.2) \times 10^6$ and freestream speeds of 10 m/s, 30 m/s, and 93 m/s is investigated symmetrically to reveal nanosecond DBD actuation mechanism. Simulation is performed within a loosely coupled numerical framework where a well validated self-similar plasma model is incorporated into a 2D RANS equations solver, whereas experiment is conducted for the low Re flows at $\mathrm{Re} = (0.05, 0.15) \times 10^6$. The transient flow actuation procedure produced by a nanosecond plasma actuator is captured with a dynamic PIV system possibly for the first time and is reproduced and complemented by detailed simulation, which is also lacking in the literature.

There are two possible control mechanisms of nanosecond actuator: exciting inherent flow instability and promoting laminar to turbulent transition of boundary layer. Both simulation and experiment show that initially the residual heat-induced spanwise vortices entrain freestream flow into the separation region over the suction surface, destroy the original shear layer, and reattach separated flow to the airfoil surface, regardless of what attack angle and Reynolds number are. After the preliminary flow reattachment, the nanosecond actuator may function in different ways, depending on both AoA and Re. This device continues generating spanwise vortices by triggering flow instability at intermediate and high poststall AoA (usually $\mathrm{AoA} > \alpha_{\mathrm{stall}} + 2^{\mathrm{o}}$), and the controlled flow features a train of repetitive, downstream moving vortices over the suction surface. By contrast, for a narrow range of AoA near stall angle (usually $\alpha_{\mathrm{stall}} \leqslant \mathrm{AoA} \leqslant \alpha_{\mathrm{stall}} + 2^{\mathrm{o}}$), the nanosecond discharge seems to perform as an active trip, promoting the transition to turbulence, and the controlled flow appears to be fully attached except for that near leading and trailing edges. It is the residual heat rather than shock wave that induces spanwise vortices and further plays a major role in the flow control. The propagation of shock wave through external flow arising from discharge has a transient effect on flow field only and contributes little to control authority. As a result, this type of actuator serves as a "moving perturbation source" as its influence region can be extended with the advection of residual heat. This effectiveness and flexibility of the nanosecond actuator may stem from this feature that traditional actuator does not have.

The benefits of flow control are twofold: significant lift enhancement and drag reduction. For example, the predicted and measured lift and drag coefficient curves are in good agreement at $\mathrm{Re} = 0.15 \times 10^6$ (30 m/s). The simulation shows that the actuation results in an average 34% increase in lift and an average 50% decrease in drag over the poststall AoA range $14^{\mathrm{o}} \leqslant \mathrm{AoA} \leqslant 24^{\mathrm{o}}$. Meanwhile, the control authority also varies with Re.

APPENDIX

1. Validation of plasma model

The experiment of a single nanosecond pulse discharge in quiescent air conducted in Ref. [35] is reproduced to validate the self-similar plasma model and illustrate characteristics of induced flow. The 2D simulation is performed in the x-y plane in Fig. 1(a). The computational domain is 5 cm wide and 2 cm high and discretized into a structured quadrilateral mesh of 600×400 with local refinement in actuator region. The flow induced by the discharge is assumed to be laminar and the turbulence model in computational fluid dynamics (CFD) code is turned off in simulation. The total coupled energy per unit actuator length predicted with plasma model (1) is $\widehat{\mathbf{Q}}_{\mathrm{couple}} = 0.179$ mJ/cm for the pulse with peak voltage of $U_p = 10$ kV and rise time of $\tau_r = 50$ ns.

The experimental and numerical schlieren images at $t = 15\ \mu$s are compared in Fig. 25, where each image depicts a wave structure composed of a cylindrical shock centered at the interface of two electrodes as well as a planar one. The shock geometries presented in the two images are in good qualitative agreement. To examine the effect of shock propagation on surrounding air, the pressure increase relative to ambient condition and y velocity component are sampled along vertical monitoring line $x = 0$, which is drawn in Fig. 25(b), and plotted in Fig. 26(a) for different times. The rapid diminishment of peak-to-peak value of pressure increase implies that the shock decays very

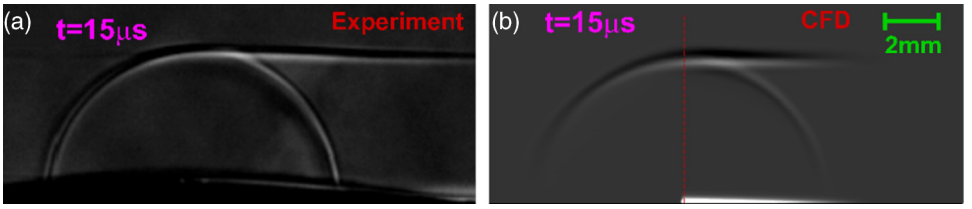

FIG. 25. Experimental (a) and numerical (b) Schlieren images for the shock wave arising from a single pulse discharge in quiescent air with $U_p = 10\,\mathrm{kV}$, $\tau_r = 50\,\mathrm{ns}$. The red dashed line drawn in plot (b) is the vertical monitoring line $x = 0$. The left subfigure is reproduced from Dawson and Little [35], with the permission of AIP Publishing.

fast as it moves outwards. Also observed is that the flow state of region swept by the shock quickly recovers to close to its undisturbed condition and the perturbation introduced by shock is restricted to a narrow region behind shock front. In other words, the perturbation exhibits highly transient and localized characteristics. This is also confirmed in the velocity field at $t = 40\,\mu\mathrm{s}$ in Fig. 26(b) where the velocity of bulk gas behind shock is close to 0. These results demonstrate again that the nanosecond DBD actuation mechanism relies mainly on discharge-caused thermal effect, rather than momentum transfer. The simulation indicates that our method based on self-similar plasma model can reproduce the principal qualitative and quantitative features of DBD actuator, which provides a basis for a reliable prediction of flow separation control.

2. Grid independence study

As an example of grid independence study, the baseline flow over the NACA0015 airfoil is considered with AoA $= 20^o$ and $\mathrm{Re} = 1.2 \times 10^6$ ($U_\infty = 93\,\mathrm{m/s}$, $c = 20.32\,\mathrm{cm}$). Relevant parameters are listed in Case C of Table I. O-type structured mesh is employed, and an example of such mesh of 1150×300 (circumferential $\times$ normal) is shown in Fig. 27. No-slip and far-field boundary conditions are imposed on the airfoil surface and outer boundary located around $20c$ away from the surface of airfoil, respectively. A grid convergence study is performed on three sets of mesh, i.e., 950×150, 1150×300, and 1350×400, which are generated in such a way that y^+ in the first layer of grid adjacent to airfoil surface is maintained at around 1 for each mesh. Simulation starts with a uniform flow condition, and after the initial transient stage, the solution evolves into a quasiperiodic state for which time-dependent lift coefficients are compared in Fig. 27(c) for three meshes. It is seen that the results obtained with fine and medium meshes are in good agreement and show discrepancy with that on the coarse one in terms of lift fluctuation and approximate period. The comparison between three meshes for separation point location and Strouhal number of wake vortex shedding (not

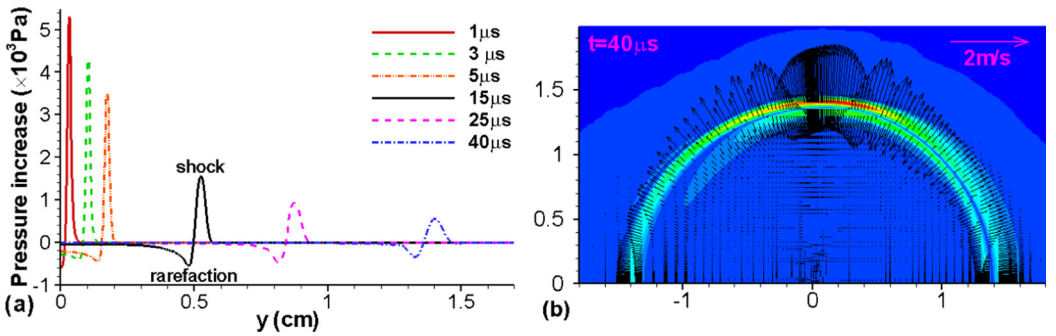

FIG. 26. Plot (a) shows profile of pressure increase along vertical monitoring line drawn in Fig. 25(b) at different times for the case shown in Fig. 25, while plot (b) depicts contour of velocity magnitude overlaid with velocity vector at time $t = 40\,\mu\mathrm{s}$.

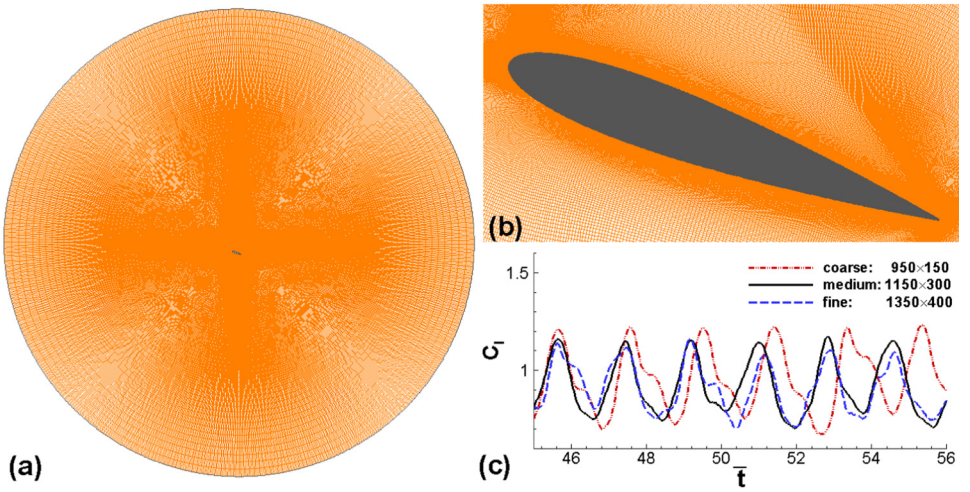

FIG. 27. Structured mesh of 1150 × 300 (circumferential × normal) around a NACA0015 airfoil with chord length $c = 20.32$ cm and angle of attack AoA $= 20^o$ (a) as well as its close-up view near airfoil surface (b). Plot (c) shows the comparison of time histories of predicted lift coefficients from three sets of grid for baseline flow at Re $= 1.2 \times 10^6$ (93 m/s), AoA $= 20^o$. Time is nondimensionalized as $\bar{t} = tU_\infty/c$ with U_∞ being freestream speed.

shown here) produces the same result. Thus, the independence of solution on grid is believed to have been reached, and the medium grid, 1150 × 300, is used in all the calculations with Re $= 1.2 \times 10^6$ in Sec. IV C. For low Re flow in Sect. IV B, a similar grid convergence study is conducted.

[1] M. Forte, J. Jolibois, J. Pons, E. Moreau, G. Touchard, and M. Cazalens, Optimization of a dielectric barrier discharge actuator by stationary and non-stationary measurements of the induced flow velocity: Application to airflow control, Exp. Fluids **43**, 917 (2007).
[2] D. V. Roupassov, A. A. Nikipelov, M. M. Nudnova, and A. Yu. Starikovskii, Flow separation control by plasma actuator with nanosecond pulsed-periodic discharge, AIAA J. **47**, 168 (2009).
[3] J. G. Zheng, Z. J. Zhao, J. Li, Y. D. Cui, and B. C. Khoo, Numerical simulation of nanosecond pulsed dielectric barrier discharge actuator in a quiescent flow, Phys. Fluids **26**, 036102 (2014).
[4] K. Takashima, Y. Zuzeek, W. R. Lempert, and I. V. Adamovich, Characterization of a surface dielectric barrier discharge plasma sustained by repetitive nanosecond pulses, Plasma Sources Sci. Technol. **20**, 055009 (2011).
[5] N. Benard, N. Zouzou, A. Claverie, J. Sotton, and E. Moreau, Optical visualization and electrical characterization of fast-rising pulsed dielectric barrier discharge for airflow control applications, J. Appl. Phys. **111**, 033303 (2012).
[6] R. A. Dawson and J. Little, Effects of pulse polarity on nanosecond pulse driven dielectric barrier discharge plasma actuators, J. Appl. Phys. **115**, 043306 (2014).
[7] Z. J. Zhao, J. Li, J. G. Zheng, Y. D. Cui, and B. C. Khoo, Study of shock and induced flow dynamics by pulsed nanosecond DBD plasma actuators, AIAA J. **53**, 1336 (2015).
[8] G. Correale, T. Michelis, D. Ragni, M. Kotsonis, and F. Scarano, Nanosecond-pulsed plasma actuation in quiescent air and laminar boundary layer, J. Phys. D **47**, 105201 (2014).

[9] C. Rethmel, J. Little, K. Takashima, A. Sinha, I. Adamovich, and M. Samimy, Flow separation control using nanosecond pulse driven DBD plasma actuators, Int. J. Flow Control **3**, 213 (2011).
[10] J. Little, K. Takashima, M. Nishihara, I. Adamovich, and M. Samimy, Separation control with nanosecond-pulse-driven dielectric barrier discharge plasma actuators, AIAA J. **50**, 350 (2012).
[11] K. Kato, C. Breitsamter, and S. Obi, Flow separation control over a GÖ 387 airfoil by nanosecond pulse-periodic discharge, Exp. Fluids **55**, 1795 (2014).
[12] G. Correale, T. Michelis, and M. Kotsonis, NS-DBD plasma actuation on a backward facing step, *52nd Aerospace Sciences Meeting, 13–17 January 2014, National Harbor, Maryland*, AIAA paper 2014-0325 (AIAA, Reston, 2014).
[13] R. Lehmann, D. Akins, and J. Little, Effects of Ns-DBD plasma actuators on turbulent shear layers, *7th AIAA Flow Control Conference, 16–20 June 2014, Atlanta, GA*, AIAA paper 2014-2220 (AIAA, Reston, 2014).
[14] C. L. Kelley, P. O. Bowles, J. Cooney, C. He, T. C. Corke, B. A. Osborne, J. S. Silkey, and J. Zehnle, Leading-edge separation control using alternating-current and nanosecond-pulse plasma actuators, AIAA J. **52**, 1871 (2014).
[15] H. Du, Z. W. Shi, K. M. Cheng, G. N. Li, J. C. Lu, Z. Li, and L. Hu, The study of flow separation control by a nanosecond pulse discharge actuator, Exp. Thermal Fluid Sci. **74**, 110 (2016).
[16] M. Nishihara, K. Takashima, J. W. Rich, and I. V. Adamovich, Mach 5 bow shock control by a nanosecond pulse surface dielectric barrier discharge, Phys. Fluids. **23**, 066101 (2011).
[17] T. Unfer and J. P. Boeuf, Modelling of a nanosecond surface discharge actuator, J. Phys. D **42**, 194017 (2009).
[18] C. C. Wang and S. Roy, Energy and force prediction for a nanosecond pulsed dielectric barrier discharge actuator, J. Appl. Phys. **111**, 103302 (2012).
[19] Y. F. Zhu, Y. Wu, W. Cui, Y. H. Li, and M. Jia, Modelling of plasma aerodynamic actuation driven by nanosecond SDBD discharge, J. Phys. D **46**, 355205 (2013).
[20] D. V. Gaitonde and M. H. McCrink, A semi-empirical model of a nanosecond pulsed plasma actuator for flow control simulations with LES, *50th AIAA Aerospace Sciences Meeting including the New Horizons Forum and Aerospace Exposition, 09–12 January 2012, Nashville, Tennessee*, AIAA paper 2012-0184 (AIAA, Reston, 2012).
[21] D. V. Gaitonde, Analysis of plasma-based flow control mechanisms through large-eddy simulations, Comput. Fluids **85**, 19 (2013).
[22] Z. L. Chen, L. Z. Hao, and B. Q. Zhang, A model for nanosecond pulsed dielectric barrier discharge (NSDBD) actuator and its investigation on the mechanisms of separation control over an airfoil, Sci. China Tech. Sci. **56**, 1055 (2013).
[23] K. Takashima, Z. Y. Yin, and I. V. Adamovich, Measurements and kinetic modeling of energy coupling in volume and surface nanosecond pulse discharges, Plasma Sources Sci. Technol. **22**, 015013 (2013).
[24] J. Blazek, *Computational Fluid Dynamics: Principles and Applications* (Elsevier Science, Oxford, 2001).
[25] A. Montello, D. Burnette, M. Nishihara, W. R. Lempert, and I. V. Adamovich, Dynamics of rapid localized heating in nanosecond pulse discharges for high speed flow control, J. Fluid Sci. Technol. **8**, 147 (2013).
[26] S. B. Leonov, V. Petrishchev, and I. V Adamovich, Dynamics of energy coupling and thermalization in barrier discharges over dielectric and weakly conducting surfaces on μs to ms time scales, J. Phys. D **47**, 465201 (2014).
[27] S. Lanier, I. Shkurenkov, I. V Adamovich, and W. R. Lempert, Two-stage energy thermalization mechanism in nanosecond pulse discharges in air and hydrogen-air mixtures, Plasma Sources Sci. Technol. **24**, 025005 (2015).
[28] J. Z. Wu, X. Y. Lu, A. G. Denny, M. Fan, and J. M. Wu, Post-stall flow control on an airfoil by local unsteady forcing, J. Fluid Mech. **371**, 21 (1998).
[29] B. E. Launder, G. J. Reece, and W. Rodi, Progress in the development of a Reynolds-stress turbulence closure, J. Fluid Mech. **68**, 537 (1975).
[30] D. C. Wilcox, *Turbulence modeling for CFD* (DCW Industries, La Cafiada, CA, 2006).
[31] *OpenFOAM User Guide*, http://cfd.direct/openfoam/user-guide/
[32] *FLUENT 6.3 User's Guide* (Fluent Inc., New York, 2006).

[33] See Supplemental Material at http://link.aps.org/supplemental/10.1103/PhysRevFluids.1.073501 for the low Re case from experiment and the high Re case from simulation.
[34] R. R. Kleinman, D. J. Bodony, and J. B. Freund, Shear-flow excitation mechanisms of recessed localized arc-filament plasma actuators, Phys. Fluids. **22**, 116103 (2010).
[35] R. Dawson and J. Little, Characterization of nanosecond pulse driven dielectric barrier discharge plasma actuators for aerodynamic flow control, J. Appl. Phys. **113**, 103302 (2013).